

# Strong Amplification of ELF/VLF Signals in Space Using Neutral Gas Injections from a Satellite Rocket Engine

Paul Bernhardt<sup>1</sup>, William Bougas<sup>2</sup>, Michael Griffin<sup>2</sup>, Chris Watson<sup>3</sup>, Richard B. Langley<sup>4</sup>, Andrew David Howarth<sup>5</sup>, H. Gordon James<sup>6</sup>, Carl Siefring<sup>1</sup>, Gareth William Perry<sup>7</sup>, J.D. Huba<sup>8</sup>, Robert Christian Moore<sup>9</sup>, Morris B. Cohen<sup>10</sup>, and Mark Golkowski<sup>11</sup>

<sup>1</sup>Naval Research Laboratory

<sup>2</sup>MIT Lincoln Laboratory

<sup>3</sup>University Corporation for Atmospheric Research

<sup>4</sup>University of New Brunswick

<sup>5</sup>University of Calgary

<sup>6</sup>Residence

<sup>7</sup>New Jersey Institute of Technology

<sup>8</sup>Syntek Technologies

<sup>9</sup>University of Florida

<sup>10</sup>Georgia Institute of Technology

<sup>11</sup>University of Colorado Denver

November 22, 2022

## Abstract

The first demonstration of rocket exhaust driven amplification (REDA) of whistler mode waves occurred on 26 May 2020 by transferring energy from pickup ions in a rocket exhaust plume to EM waves. The source of coherent VLF waves was the Navy NML Transmitter at 25.2 kHz located in LaMoure, North Dakota. The topside ionosphere at 480 km altitude became an amplifying medium with a 60 second firing of the Cygnus BT-4 engine. The rocket engine injected exhaust as a neutral cloud moving perpendicular to field lines that connected the NML transmitter to the VLF Radio Receiver Instrument (RRI) on e-POP/SWARM-E. Charge exchange between the ambient  $O^+$  ions and the hypersonic water molecules in the exhaust produced  $H_2O^+$  ions in a ring-beam velocity distribution. The 25.2 kHz VLF signal from NML was amplified by 30 dB for a period 77 seconds as observed by the RRI. Simultaneously, preexisting coherent ELF waves at 300 Hz were amplified by 50 dB during and after the Cygnus burn. Extremely strong coherent emissions and quasi-periodic bursts in the 300 to 310 Hz frequency range lasted for 200 seconds after the release. The excitation of an ELF whistler cavity may have lasted even longer, but the orbit of the SWARM-E/e-POP moved the RRI sensor away from the wave emission region. The amplified 300 Hz ELF waves may have gained even more energy by cyclotron resonance with radiation belt electrons as they were ducted between geomagnetic-conjugate hemispheres.



43 [Borovsky and Delzanno, 2019] for space-based VLF wave generation are supported in the United States  
44 by (1) the Air Force Research Laboratory with the DSX large dipole antenna operational from June 2019  
45 to transmit VLF waves in space [Scherbarth et al., 2009], (2) the Los Alamos National Laboratory with a  
46 VLF precipitation experiment scheduled for April 2021 to launch the Beam Plasma Interactions Experiment  
47 (Beam-PIE) with electron beam generation on a sounding Rocket [Carlsten et al., 2019], and (3) the Naval  
48 Research Laboratory with an injection of 1.5 kg of barium to form hypersonic ions that are converted into  
49 lower-hybrid, whistler or magnetosonic waves [Ganguli et al., 2015, Ganguli et al., 2019]. Alternate  
50 techniques for whistler mode generation are being studied because these waves are difficult to radiate  
51 with conventional antennas where the free space wavelengths (10–1000 km) are so much longer than a  
52 practically realizable vertical monopole antenna, and the radiation efficiency is exceedingly small.

53 The VLF wave sources are expensive in terms of ground facility or spacecraft launch and maintenance  
54 costs. There is an on-going debate over which system has the most efficiency (Carlsten et al., 2019; Ganguli  
55 and Crabtree, 2020; Carlsten et al., 2020). Engineering design and state-of-the-art innovation for these  
56 systems adds both cost and risk to each system. In addition, each space-based device has built-in  
57 inefficiencies that increase both launch and design costs. The RF driven-antenna-in-space concept such  
58 DSX requires extremely large currents (for a loop antenna) or extremely large voltages (for dipole  
59 antennas) because it is difficult to efficiently launch VLF waves with wavelengths much larger than the  
60 physical devices. The electron beam system (Beam-PIE) requires flying a particle accelerator with only a  
61 fraction of the payload mass devoted to the electron beam itself. Finally, the ion beam chemical release  
62 of barium [Ganguli et al., 2019] uses thermite vaporization system that is typically ten-times more massive  
63 than the amount of barium gas released.

64 This paper presents a simple, low-cost alternate concept where the space plasma medium is converted to  
65 an amplifier (as opposed to generator) of large-amplitude VLF waves in the ionosphere. These amplified  
66 waves propagate to the magnetosphere as left-hand circularly polarized whistlers. This newly proposed  
67 technique thus converts the earth's plasma medium into a whistler mode amplifier. This work  
68 demonstrates that a large area region in space can greatly enhance the amplitude of whistler waves from  
69 either ground-based or space-based sources. This new concept for an ELF/VLF wave generation system is  
70 thus broken into three components consisting of (1) a localized ELF/VLF wave exciter or generator on the  
71 ground or in space, (2) a high-gain amplifier involving an efficient chemical injection that is distributed  
72 through the medium of space, and finally (3) the radiation belt region where further amplification can  
73 occur along with the generation of broad-band noise by interaction with radiation belt electrons. The  
74 generation component using ground and space-based transmitters has been the focus of the many  
75 previous studies described above. The distributed-region amplifier proposed here has never been  
76 previously considered by either experiment or theory. The new concept demonstrated in this paper is  
77 that neutral gas jets from a rocket motor can form a large-area amplification region in space. The process  
78 of rocket exhaust driven amplification (REDA) for coherent VLF waves employ hypersonic molecules from  
79 exhaust jets to charge exchange in the ionosphere yielding gyrating ion beams. These beams transfer  
80 energy to whistler mode waves for extremely strong amplification. The amplifier acts for a finite period  
81 (about minutes) to inject intense VLF waves along magnetic field lines into the magnetosphere. Wave  
82 amplification should accompany scattering of the radiation belt population into the loss-cone through a  
83 process called chemical-release-induced electron precipitation (cep).

84 For the past 11 years, the Naval Research Laboratory has conducted the Spacecraft Exhaust Ion  
85 Turbulence Experiment (SEITE I and II) aimed at providing multiple measurements of rocket engine burns

86 leading to excitation and/or amplification of low frequency plasma waves in the space environment. The  
 87 science objectives of the SEITE missions are (1) to advance physical understanding of artificial ion-ring  
 88 beam generation by charge exchange with hypersonic neutral jets leading to the excitation of plasma  
 89 waves, (2) to identify the electrostatic, MHD, and whistler-mode wave generation mechanisms from  
 90 neutral gas injections in the ionosphere leading to enhanced noise on space sensors with comparison to  
 91 ambient plasma wave noise in the plasmasphere, and (3) to evaluate dedicated rocket motor firings for  
 92 launching whistler waves to study interactions with the charged particle environment in the  
 93 magnetosphere. The SEITE I experiments had previously dedicated burns of the OMS engines on the  
 94 Space Shuttle in conjunction with the plasma sensors (VEFI, CINDI and PLP) on the AFRL C/NOFS satellite  
 95 [Bernhardt et al., 2012].

96 The current SEITE II experiments are employing the BT-4 engine on the Cygnus spacecraft in conjunction  
 97 with the e-POP suite of instruments (RRI, GAP, and MGF) on the SWARM-E/CASSIOPE spacecraft.  
 98 Maxworth, A., Glenn Hussey and Mark Golkowski [2020] have reviewed use of the radio receiver  
 99 instrument (RRI) to monitor VLF waves excited by natural sources. The first SEITE II experiment showed  
 100 RRI detection of enhanced finite- $k_z$  Lower Hybrid waves during a 30-second burn from the BT-4 engine.  
 101 This first experiment occurred on 22 July 2018 at a range of 50 km between Cygnus and e-POP during the  
 102 OA-9E Mission [Bernhardt et al., 2020]. The OA-9E Cygnus burn did not have any effect on the 19.8 kHz  
 103 VLF waves from the powerful VLF station NWC located 5630 km from the burn. The second SEITE II test  
 104 was executed on 26 May 2020 during the NG-13 flight of Cygnus with the specific objective of greatly  
 105 enhancing the power of existing VLF waves in the topside ionosphere. In this second case, the burn  
 106 occurred directly over the NML VLF station broadcasting at 25.2 kHz and the observed wave amplification  
 107 was between 20 and 30 dB. The next sections describe the first successful demonstration of rocket  
 108 exhaust driven amplification (REDA) followed by supporting theory and modeling of changes in the  
 109 ambient plasma environment leading to VLF wave-amplification.

110 **2. The SEITE II Test of Rocket exhaust driven amplification during the NG-13 Cygnus Mission**

111 The second SEITE II experiment was designed to investigate the REDA technique by firing a rocket motor  
 112 on a satellite in conjunction with an existing VLF wave source on the ground. The concept for the ELF/VLF  
 113 wave amplification process is based on several steps to go from a ground transmitter to a large amplitude  
 114 whistler propagating into the magnetosphere. First, a monochromatic VLF, which is transmitted into  
 115 space from a ground station, has been observed to change from linear into circular polarization (i.e., a  
 116 whistler mode) on its path through the neutral atmosphere and into the ionosphere [Kintner et al., 1983].  
 117 The whistler mode propagates unamplified until it reaches the ion-ring distribution region setup by ion-  
 118 molecule charge exchange in a rocket exhaust plume. Finally, the artificially amplified waves are guided  
 119 into the radiation-belt region as whistler mode for further intensification by wave-particle interactions. A  
 120 diagram of the concept is given in Figure 1.

121

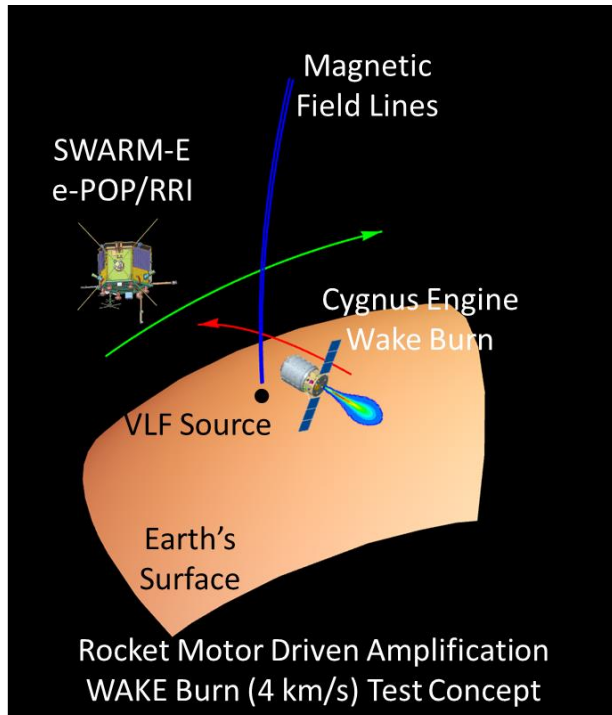


Figure 1. Detailed configuration of the NG-13 Cygnus engine operation to yield the injection velocities perpendicular to a (blue) magnetic field line with wake burn. The Cygnus spacecraft is moving horizontally along the red trajectory. The injection speed determines the kinetic energy of the ions created by the charge exchange process in the ionosphere. The plasma wave observations with the RRI on SWARM-E (green trajectory) will be made during the REDA tests with enough energy to form a ring-beam ion velocity distribution that can promote EM wave amplification.

138

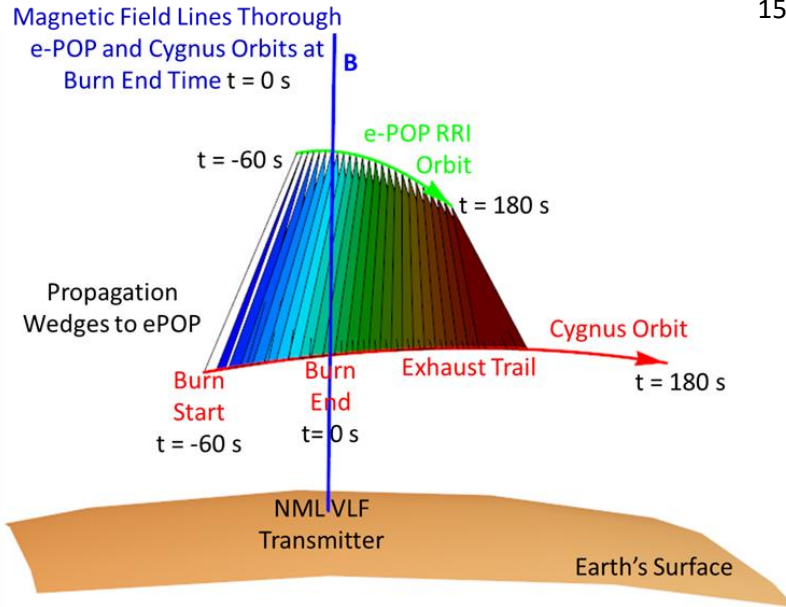
139 This test of REDA used the BT-4 on the Cygnus spacecraft that serviced the ISS during the NG-13 Mission.  
 140 The single BT-4 thruster produces 450 N of thrust by burning a mixture of NTO and Hydrazine ( $N_2O_4$  (97%)  
 141 + NO (3%) +  $N_2H_4$ ). This combustion yields a number of molecular exhaust products according to the  
 142 reaction



144 The BT-4 rocket yields an exhaust velocity of 3185 m/s with a flow rate of 0.147 kg/s.

145 The NC-13 Cygnus was launched on 15 February 2020 and reentered the Earth's atmosphere on 29 May  
 146 2020. After Cygnus undocked from the Space Station on 11 May 2020, it went into a free-flyer mode  
 147 performing a number of experiments including the NRL SEITE II burn starting on 26 May 2020 at 00:13:20  
 148 with a 60-second burn of the BT-4 engine. The burn end time (00:14:20 UT) was chosen to occur when  
 149 the exhaust source (Cygnus) was between a ground VLF transmitter (NML) and the plasma sensor satellite  
 150 (e-POP) on the same magnetic line (Figure 2). This experiment geometry allowed amplification of the  
 151 whistler mode waves generated by the 25.2 kHz radio emissions from NML US Navy Transmitter at La  
 152 Moure, North Dakota that couple through the bottomside ionosphere to reach the Cygnus orbit.

153



154 Figure 2. Cygnus-e-POP burn on 26 May 2020 for a magnetic field line conjunction with the NML VLF transmitter on the ground. The amplified emissions from the exhaust trail regions propagate in the triangles to the e-POP Radio Receiver Instrument at a higher altitude orbit. The 60 s BT-4 Burn was terminated at 00:14:26 UT when the Cygnus orbit contacted the magnetic field line (**B**) that crossed the orbit e-POP 20 seconds later. At that time, the altitudes of Cygnus and e-POP were 481 km and 1063 km, respectively.

171 The NML transmitter radiates continuously with 250 to 500 kW power and a 300 Hz FSK modulation for  
 172 communications to submerged submarines. The 25.2 kHz VLF waves must first pass through the region  
 173 of BT-4 exhaust cloud to reach the VLF receiver of e-POP. For this experiment, the e-POP/RRI was  
 174 observing wave emissions in the 10 Hz to 35 kHz frequency range. The RRI instrument is connected to a  
 175 pair of 6-m dipoles denoted as channels A and B [James, 2006; James et al. 2015]. The dipoles are located  
 176 on the ram face of the spacecraft at 45 degrees to the orbit plane. The Cygnus spacecraft was moving at  
 177 7.3 km/s while the e-POP orbit speed was 7.7 km/s, both nearly perpendicular to the magnetic field line.  
 178 The BT-4 nozzle was pointed in the ram direction of the Cygnus orbit for a posigrade burn that injects the  
 179 exhaust with a speed of  $7.3 - 3.1 = 4.2$  km/s. This orientation placed the exhaust cloud moving across the  
 180 magnetic field line at the time of intersection by the e-POP instruments.

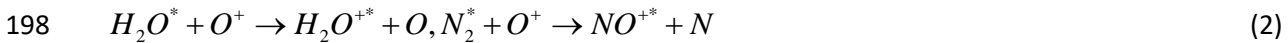
181 The NG-13 Cygnus burn occurred at an altitude chosen to have sufficient ambient  $O^+$  ions to charge  
 182 exchange with the injected wave vapor and for geographic location above a ground VLF transmitter. The  
 183 locations of the two satellites in both geographic and geomagnetic coordinates are given in **Table I**. The  
 184 end of the Cygnus burn was located near a single magnetic field line containing the e-POP orbit and was  
 185 almost directly above the 25.3 kHz VLF transmitter located at  $46.366^\circ$  N Latitude and  $-98.3367^\circ$  E  
 186 Longitude. **Table I** also provides the in situ values of electron densities based on GPS TEC measurements  
 187 and models as explained in Section 5.

188  
 189  
 190  
 191  
 192

193 **Table I. Geographic, Geomagnetic and Plasma Parameters of the Cygnus and e-POP/SWARM-E**  
 194 **Satellites for the NG-13 Burn during Second SEITE II Experiment**

| Parameter                               | Burn Start | Burn End |
|---|------------|----------|
| Time (H:M:S GMT)                        | 00:13:20   | 00:14:20 |
| Cygnus Altitude (km)                    | 480.3      | 480.9    |
| Cygnus Longitude (°E)                   | -102.7     | -98.5    |
| Cygnus Latitude (°N)                    | 41.7       | 43.8     |
| Cygnus L Shell                          | 2.39       | 2.61     |
| Cygnus Magnetic Longitude (°E)          | -27.1      | -22.6    |
| Cygnus $N_e$ ( $10^4 \text{ cm}^{-3}$ ) | 8.3        | 8.3      |
| ePOP Altitude (km)                      | 1040.4     | 1063.9   |
| ePOP Longitude (°E)                     | -99.7      | -98.8    |
| ePOP Latitude (°N)                      | 47.3       | 44.1     |
| ePOP L Shell                            | 3.31       | 2.85     |
| ePOP Magnetic Longitude (°E)            | -24.6      | -23.6    |
| ePOP $N_e$ ( $10^4 \text{ cm}^{-3}$ )   | 0.82       | 0.77     |

195  
 196 The proposed mechanism for VLF wave amplification is to have Cygnus inject exhaust perpendicular to B  
 197 and produce charge exchange with the ambient oxygen ions with the reactions



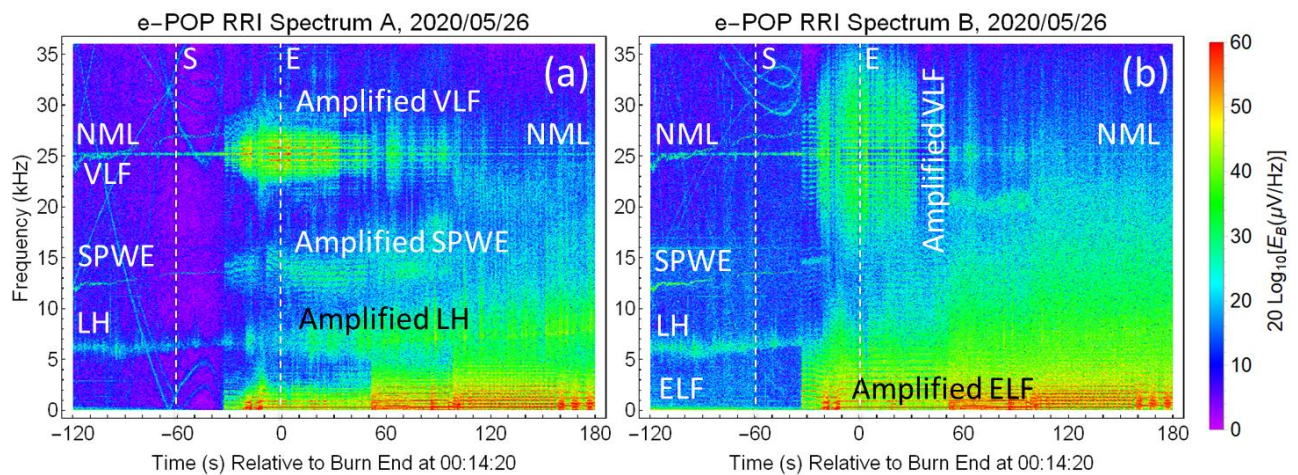
199 The resulting pickup ions form into a ring-beam distribution with perpendicular ion motion near 4 km/s.  
 200 The ring-beam distribution, previously measured with incoherent scatter radar from a Space Shuttle OMS  
 201 burn by Bernhardt and Sulzer [2004], can excite a variety of plasma oscillations including Lower Hybrid  
 202 waves and Fast MHD/Alfven Waves. The Lower Hybrid wave may act as a pump for Parametric  
 203 Amplification of the whistler mode provided by the ground NML transmitter. This amplified wave then  
 204 propagates along the magnetic field line as a whistler mode to be observed 580 km higher in altitude by  
 205 the RRI electric field sensors. Other mechanisms for amplification of whistler waves by interaction with  
 206 energetic electrons have been proposed by Lee and Crawford [1970]. With these parametric or electron-  
 207 interaction amplification processes in mind, the SEITE II/REDA experiment was conducted employing orbit  
 208 planning and burn execution by Northrup Grumman, NASA and MIT/LL during the NG-13 flight of Cygnus.  
 209 Besides the RRI on e-POP, the magnetometer (MGF) observed magnetic field changes and the GPS  
 210 occultation (GAP-O) and Attitude (GAP-A) receivers obtained data on the total electron content (TEC) to  
 211 6 GPS satellites.

212 The geometry for the NG-13 SEITE experiment is shown in Figure 2. VLF signals generated on the ground  
 213 by the NML transmitter become amplified as they passed through the exhaust trail along the Cygnus orbit.  
 214 To reach the position of the VLF receiver (RRI) on the e-POP orbit, the waves must travel along the colored  
 215 triangular wedges shown in the figure. For whistler mode, this propagation from the pickup-ion trail to  
 216 receiver occurs if the line-of-site paths make an angle of 19.6 degrees or less with the magnetic field lines

217 [Storey, 1953; Swanson, 1989]. For the NG-13 Cygnus flight geometry, this condition lasts for about 60  
 218 seconds after the burn termination time. In summary, detection of amplified VLF waves by the RRI on e-  
 219 POP require (1) energy transfer from the gyrating pickup ions in the Cygnus exhaust trail, and (2)  
 220 approximate alignment of the propagation paths with the earth’s magnetic field lines.

221 **3. RRI Measurements of the NG-13 VLF Wave Amplification for SEITE II**

222 The VLF waves recorded by the RRI on e-POP showed extremely strong amplification of the 25.2 kHz  
 223 transmission (Figure 3.) along with another ambient signal at 300 Hz. In addition, the low frequency 300  
 224 Hz wave introduced harmonics in the plasma wave receiver data. Figure 3 shows an overall view of the  
 225 ELF and VLF spectrum from the A and B channels of the RRI of e-POP. Starting 10 seconds after the  
 226 initiation of the burn, the signals from NML were amplified for a period of about two minutes. Multiple  
 227 harmonic sidebands with separations near 600 Hz occurred around the 25.2 MHz VLF carrier. This region  
 228 is labeled Amplified VLF in Figures 3a and 3b for channels A and B, respectively. The ambient strong  
 229 plasma wave emission (SPWE), discovered in 2018 by Bernhardt et al. [2020], was also amplified in channel  
 230 A. Finally, ELF wave emissions with odd harmonics of 300 Hz are observed in channels A and B. The VLF  
 231 wave signal powers return to their pre-event levels at about 3 minutes after the end of the burn. In the  
 232 discussions of the data analysis and the model studies, time will be referenced to the termination of the  
 233 burn, which is also the time for Cygnus to be located on the common field line between Cygnus and e-  
 234 POP (Figure 2).



235 Figure 3. Channels A (left) and B (right) of the radio receiver instrument (RRI) on e-POP during the fly over  
 236 of the 25.2 kHz VLF NML transmitter in North Dakota. A dedicated 60-second burn of the Cygnus BT-4  
 237 thruster occurred during the times labeled as S (start) and E (end). Observational data will be referenced  
 238 to time (t) relative to the termination time (00:14:22 GMT) of the burn.  
 239

240 Each of the burn-induced features of the measured ELF/VLF spectra will be discussed separately. The 20  
 241 to 30 dB VLF amplification at 25.2 kHz shows the strongest correlation with both ignition and shut-down  
 242 of the Cygnus engine. As such, this amplification alone demonstrates success of the rocket motor driven  
 243 acceleration (REDA) concept. A discussion on amplification of the SPWE will be postponed to the future  
 244 because the source and nature of the SPWE are unknown with speculation that it is related to finite  $k_z$   
 245 lower hybrid waves [Bernhardt et al., 2020]. The amplified lower hybrid (LH) frequencies will not be  
 246 discussed here. Major focus will be devoted to the 50 dB amplification of 300 Hz ELF waves that, after the

247 initial amplification by the Cygnus burn, excited an enhancement-duct resonator that extended through  
 248 the radiation belts for further amplification.

249 The Cygnus burn established an amplifying plasma environment producing a 1000-fold power gain for the  
 250 VLF signal from NML as measured by the e-POP RRI. The 77 second portion of the amplification labeled  
 251 REDA in Figure 4 started at 00:13:45, 35 seconds after the start of the burn, and ended at 00:15:12, 52  
 252 seconds after the end of the burn. This is a period of favorable propagation for whistler mode between  
 253 the exhaust trail and the RRI as illustrated in Figure 2. Amplification is observed in exactly the region  
 254 predicted for whistler propagation from the Cygnus exhaust trail to e-POP based on the favorable  
 255 propagation angle relative to the field line vector **B**.

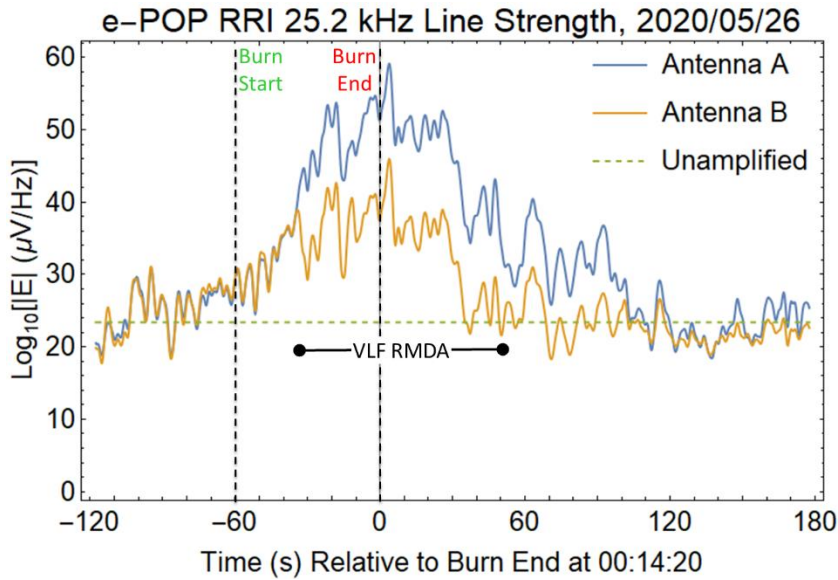


Figure 4. The measured NML carrier strength showing strong VLF amplification by whistler mode propagation through the modified ionosphere during and after the 60 second BT-4 burn of the Cygnus motor. The period of strong REDA lasted for 76 seconds.

269 The observed amplification is remarkable because of the enormous VLF power gain provided by the  
 270 plasma region energized by fast ions in the Cygnus exhaust plume. The measured gain of the REDA system  
 271 is large, but different, for each the two channels, being 34 dB for channel A and 22 dB for channel B. The  
 272 60 second burn of the BT-4 motor on Cygnus provided 9 kg of exhaust distributed over a horizontal  
 273 distance of 432 km in 60 seconds. The kinetic energy of this injection is 78 M Joules or a power of  $P_{\text{Burn}} =$   
 274 1.3 MWatts for 60 seconds. Thus, a large amount of kinetic energy is input into the ionospheric plasma  
 275 system to be available for amplifying whistler mode waves. After amplification of the signal from the 500  
 276 kW NML transmitter, the measured signal strength is equivalent to a 60-second transmission from a 500  
 277 MW ground transmitter. This is important because the estimated ELF and VLF power that can reach the  
 278 upper atmosphere from ground based systems is on the usually less than 1 Watt, up to hundreds of Watts  
 279 at best [Cohen and Golkowski, 2013].

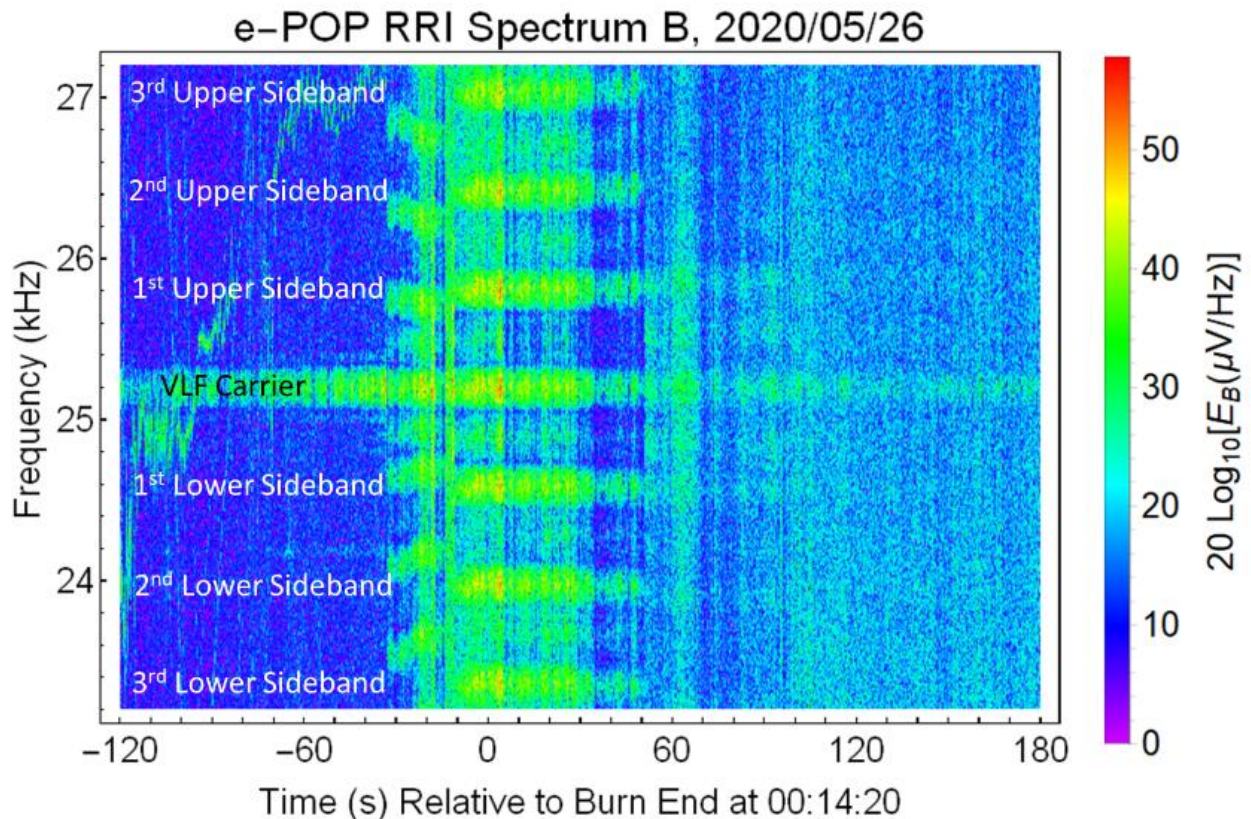
280 The estimated power in the amplified waves is given by  $P_{\text{WT}} = \frac{|E|^2 \Delta f^2}{\eta_0 n_w A_{\text{RRI}}} A_{\text{Exhaust}} = 8.5 \text{ kW}$  where E is the

281 electric field in Figure 4,  $\Delta f = 10 \text{ Hz}$  is the spectral analysis frequency bin,  $\eta_0 = 377 \text{ Ohms}$ ,  $n_w = 32$  is the  
 282 Whistler mode refractive index,  $A_{\text{RRI}} = 36 \text{ m}^2$  is the RRI Antenna area, and  $A_{\text{Exhaust}} = 10^{10} \text{ m}^2$  is the  
 283 amplification area of the Cygnus burn region. The REDA efficiency is for this experiment estimated to be  
 284  $P_{\text{WT}} / P_{\text{Burn}} = 0.5 \%$ .

285 This efficient estimate neglects the angular spreading for waves travelling between Cygnus and RRI. If the  
 286 waves are confined to a 19.6 degree cone for the length of 582 km long propagation paths, the projected  
 287 area of the exhaust cloud grows to the has been neglected for the whistler mode. If the stimulated  
 288 whistler waves radiate inside a 19.6-degree propagation cone, the projected exhaust grows to  $5 \times 10^{11} \text{ m}^2$ .  
 289 With waves spread over this area, the total power grows to 400 kW and the energization efficiency using  
 290 the measured electric field strength increases to 25%. This number will be refined with future propagation  
 291 studies using a three-dimensional model of the chemical release.

292 The temporal changes in received 25.2 kHz wave power correlate well with the burn before, during, and  
 293 after the burn event but there is about 10 dB difference between A and B in the amplification phase  
 294 (Figure 4). Before the experiment, it was expected that the power levels on those two channels would be  
 295 the same because those antennas are located at an angle of  $\pm 45$  Degrees to the plane containing the e-  
 296 POP orbit and the earth's magnetic field. Also, note that the sideband generation is significantly different  
 297 on the two RRI channels. This effect is the result of signal saturation of the RRI preamplifier and it will be  
 298 discussed in more detail later.

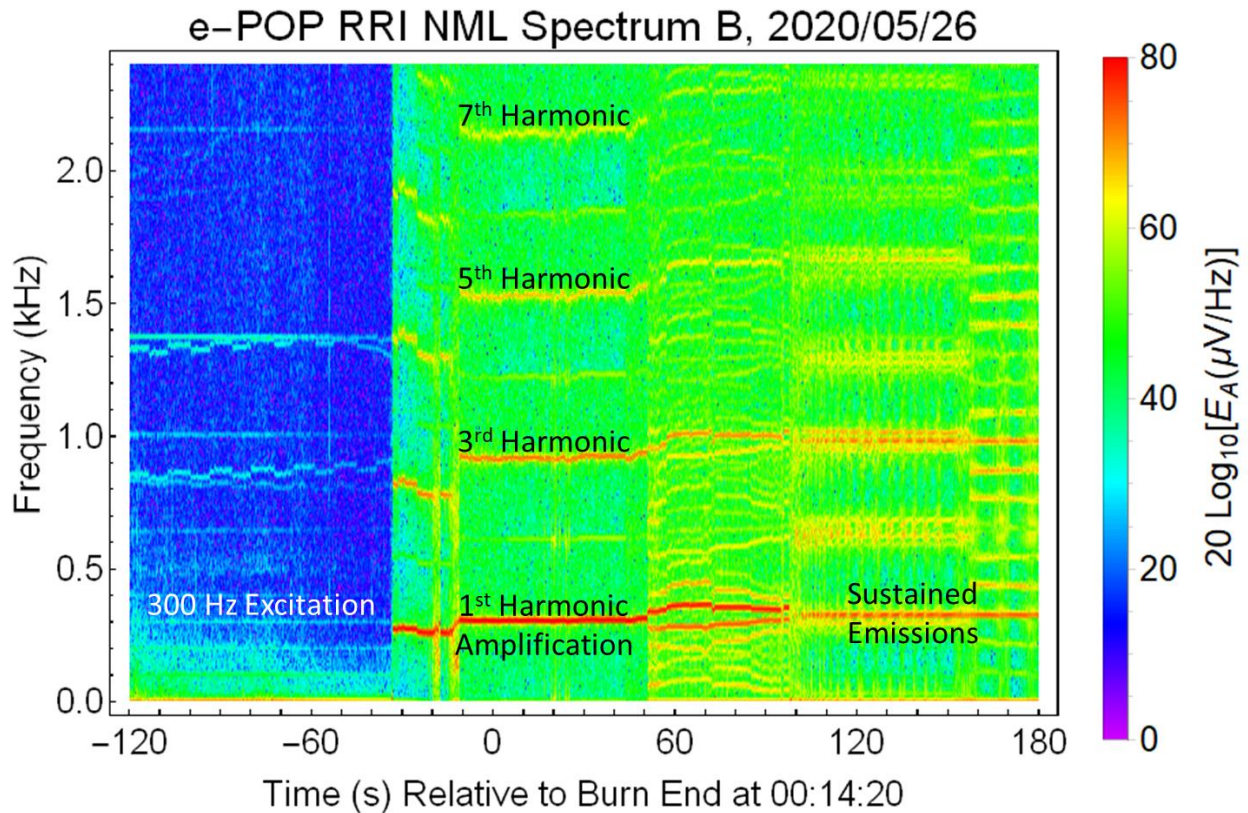
299



300 Figure 5. Symmetric sidebands around the 25.2 kHz modulated carrier signal from NML. The RRI channels  
 301 A and B contain sidebands separated by 600 Hz starting at 30 seconds after the burn starts at (00:13:20)  
 302 and lasts for 60 seconds after the burn ends. These sidebands are attributed to saturation of the RRI  
 303 preamplifier by a separate strongly amplified signal near 300 Hz seen in the spectrum of Figure 6.  
 304

305 The e-POP RRI observations show a 25.2 kHz transmission from NML that is modulated with multiple  
 306 sidebands separated by 600 Hz that extend from the carrier by multiples of  $\pm 4$  for channel A and  $\pm 15$  for

307 channel B (Figures 3 and 5). The upper and lower sidebands with power levels close to the center carrier  
 308 have the same bandwidth as the NML carrier. The Channel A sidebands extend out  $\pm 2$  kHz from the  
 309 carrier while the sampled electric fields on Channel B extend out to  $\pm 10$  kHz with about 10 dB drop in  
 310 signal strength. These sidebands are not from nonlinearities in the plasma but, based on spacecraft  
 311 engineering analysis, are from nonlinear saturation of the preamps used in the e-POP RRI. These  
 312 sidebands are the result of overdriving the input preamplifier for the RRI by a second, ELF signal at 300 Hz  
 313 that is even more strongly amplified in the active plasma cloud region of by the Cygnus burn.



314  
 315 Figure 6. Ambient harmonics of 100 Hz and other ELF signals are present in the RRI spectrum before the  
 316 60-second Cygnus burn. The ELF radio emissions, associated with harmonics of 100 Hz in the spectrum,  
 317 excite a strongly amplified wave near 300 Hz labeled 1<sup>st</sup> Harmonic. Remnants of the amplified signal  
 318 evolving into sustained split and burst modes last for more than 180 seconds after the termination of the  
 319 burn. The odd harmonics at 900, 1500, and 2100 Hz result from overdriving the preamplifier in the Radio  
 320 Receiver Instrument that recorded the data.

321 The amplification of the ELF wave at 300 Hz is much larger than the amplification for the 25.2 kHz VLF  
 322 wave. The ambient 300 Hz signal has a power level of about 30 dB $\mu$ V/Hz starting at 00:13:56, 24 seconds  
 323 before the end of the burn (Figure 6). The active plasma medium then enhances the signal power by 50  
 324 dB to 80 dB $\mu$ V/Hz maintaining a constant power for about 74 seconds. The 3<sup>rd</sup>, 5<sup>th</sup>, and 7<sup>th</sup> harmonics that  
 325 are very prominent in the spectrum are attributed to overdriving the RRL preamp. The sustained  
 326 emissions and bursts near 300 Hz 50 to 160 seconds after the end of the burn are produced by excitation  
 327 of a magnetic field aligned resonator for whistler mode that extends between hemispheres.

328 The environmentally amplified 300 Hz ELF signals couple into the RRI antennas and drive the input  
 329 preamps of the RRI into compression. This converts the sinusoidal waveform of the plasma wave into a  
 330 symmetrical square wave that is digitized by the A/D converter in the RRI. The distortion of the waveform  
 331 by the preamp is responsible for the odd harmonics at 300 Hz and the sidebands at 25.2 kHz.

332 The preamp saturation with the 300 Hz signal induces sidebands into the 25.2 kHz that are separated by  
 333 600 Hz. The preamp saturation occurs twice every 300 Hz cycle. This is equivalent to modulating the 25.2  
 334 kHz by multiplying a 600 Hz asymmetric pulse wave that transitions from full ON to OFF. In frequency  
 335 space, this represents a convolution of the 25.2 kHz with the 600 Hz harmonics in the spectrum of the  
 336 multiplication pulse. Analysis of the overdriven preamp indicates that the 300 Hz signal is compressed by  
 337 3 dB and the 25.2 Hz signal is compressed by 7 dB. All of the harmonics or harmonics modulations for  
 338 both signals are instrumental and have no origin in the excited plasma medium.

339 The amplitude of the 300 Hz ELF signal at e-POP is isolated using a 10 Hz wide tracking filter (Figure 7).  
 340 The ambient, unamplified 300 Hz wave is on the order of 30 dB $\mu$ V/Hz in channel B until it is rapidly  
 341 enhanced to 80 dB $\mu$ V/Hz by REDA. This level remains constant for 50 seconds after the Cygnus engine  
 342 shutoff. This is the same period of 30 dB amplification for the 25.2 kHz VLF signal shown in Figure 7.  
 343 Unlike the VLF frequency, the 300 ELF continues at elevate power past the REDA period. At this later time,  
 344 the ELF wave drifts in frequency, is split into several sidebands and enters into a sustained/burst mode as  
 345 labeled in Figures 6 and 7.

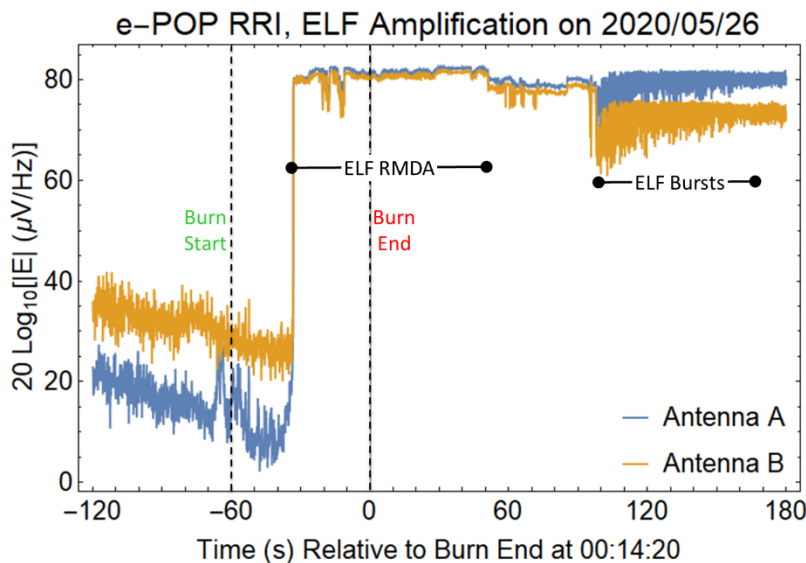


Figure 7. Amplification of the 300 Hz whistler wave by the plasma medium driven with a chemical injection of molecular rocket exhaust. The sudden increase in ELF signals on both channels A and B of the RRI occurs 28 seconds after the start of the rocket motor and it stays for more than 50 seconds after the rocket engine stops.

359 The 300 Hz wave spectra shown in Figure 6 can be broken into 3 phases. Between times of -35 seconds  
 360 and +52 seconds, the amplified ELF is monochromatic with a constant strength near 80 dB $\mu$ V/Hz. This is  
 361 the same period for amplification of the 25.2 kHz VLF mode. This period is the direct rocket exhaust driven  
 362 amplification (REDA) period. From 52 to 98 seconds after burn end, the ELF (300 Hz) spectrum breaks into  
 363 at least 4 frequency sidebands around 300 Hz. From 98 to 160 seconds, the 300 Hz signal coalesces to  
 364 one frequency with periodic noise bursts that resemble those observed with DEMETER by Hayosh et al.  
 365 [2015] in conjunction with electron precipitation. A high-resolution spectrogram of the bursts is shown  
 366 in Figure 8. These large amplitude (6 mV/Hz) signals at 330 Hz have a time separation of about 0.4 s.

367

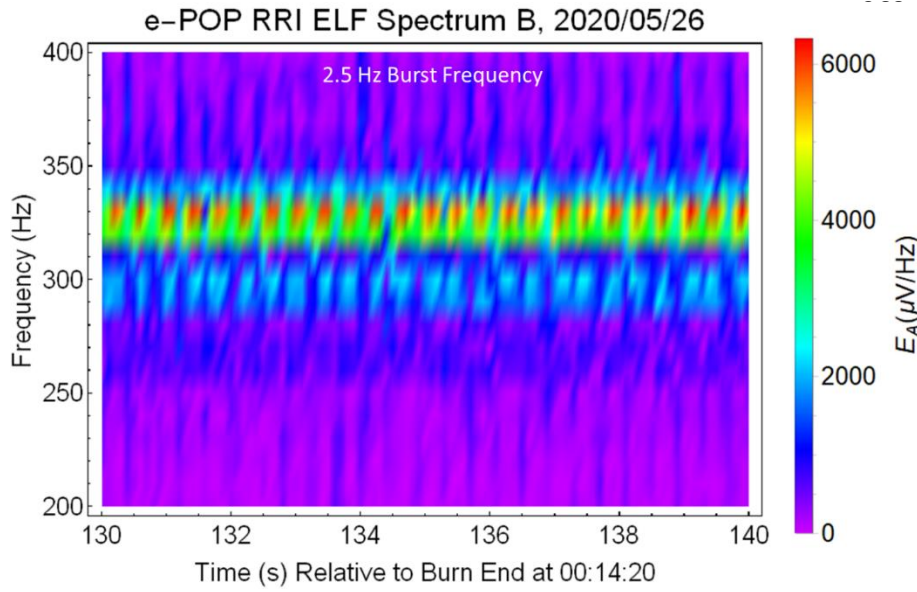


Figure 8. Cygnus burn triggered ELF noise bursts associated with late time propagation of multi-hop, ducted whistler waves following the burn of the Cygnus engine on an L = 2.8 field line.

381

382

**Table II. Cygnus-ePOP Burn and Rocket exhaust driven amplification (REDA) Observation Times**

| Time (H:M:S GMT)          | 00:13:20 | 00:14:20   | 00:13:20  | 00:13:20         | 00:13:20                | 00:13:20          |
|---------------------------|----------|------------|-----------|------------------|-------------------------|-------------------|
| Time After Burn Start     | 0        | 25 s       | 60 s      | 112 s            | 158 s                   | 220 s             |
| Time Offset from Burn End | -60 s    | -35 s      | 0 s       | 52 s             | 98 s                    | 160 s             |
| Cygnus Event              | BT-4 ON  |            | BT-4 OFF  |                  |                         |                   |
| 300-330 Hz ELF Event      |          | RMDA Start |           | 300 Hz Lock Lost | 330 Hz Lock Burst Start | 330 Hz Burst Stop |
| 25.2 kHz VLF Event        |          | RMDA Start |           | RMDA Stop        |                         |                   |
| GPS TEC Reduction         | 0 TECU   | 0 TECU     | 0.17 TECU | 0.22 TECU        | 0.20 TECU               | 0.15 TECU         |

383

384 The timing for the VLF and ELF events is summarized in Table II. Both the ELF and VLF signals are amplified  
 385 for the same time periods relative to the Cygnus engine burn ignition and termination. The ELF emissions  
 386 after amplification continue for another 108 seconds as frequency-drifting, narrowband signals and quasi-  
 387 periodic bursts with 400 ms periods. The GPS TEC reductions associated with the recombination of the  
 388 molecular pickup ions start just after the end of the burn as discussed in Section 5.

389 The VLF and ELF electric fields recorded by the RRI show (1) amplified signals that are easily observed in  
 390 the data even though the RRI preamp is over driven at ELF, (2) that the preamp compression of the 300  
 391 Hz and 25.2 kHz carriers are estimated to be 3 and 7 dB respectively, and (3) that the neutral injection  
 392 technique yields a plasma medium with 50 dB gain for 300 Hz and 30 dB gain for 25.2 kHz. A water vapor  
 393 and molecular nitrogen injection at 4.2 km/s perpendicular to **B** will charge exchange with the ambient

394 atomic oxygen ions to produce an ion-ring distribution. These measurements give convincing evidence  
 395 and demonstrate that REDA greatly enhances both ELF and VLF whistler mode waves. In the following  
 396 sections, the other e-POP sensors and a model of the orbital chemical release give more weight to this  
 397 interpretation of the NG-13 REDA experiment during SEITE II.

#### 398 4. Computational Model of the Cygnus Exhaust Release and Interactions in the Ionosphere

399 The first step in the analysis of the NG-13 Cygnus burn is to model the injected exhaust cloud and  
 400 subsequent charge exchange in the background ionosphere. The neutral gas expansion from a rocket  
 401 motor can be described by continuum, kinetic, or particle models depending on the injection altitude and  
 402 mean free path. The exhaust from Cygnus was released at 480 km altitude at a supersonic speed of 4.1  
 403 km/s relative to the background atmosphere, which has a horizontal mean free path of 460 km. Under  
 404 these conditions, the neutral expansion can be described by the following equations for collisionless  
 405 expansion into a vacuum

$$\begin{aligned}
 N_n(R, \theta, \phi, t) &= \frac{N_{D0}}{8\pi R^2 v_s} \Phi_\theta(\theta) \left\{ \operatorname{erf} \left[ \frac{R - tv_s}{\sqrt{2Rv_m/v_s}} \right] - \operatorname{erf} \left[ \frac{R - (t - \min[t, t_e])v_s}{\sqrt{2Rv_m/v_s}} \right] \right\} \\
 \text{with } \Phi_\theta(\theta) &= \frac{\operatorname{erf} \left( \frac{\theta + \theta_0}{\Delta\theta} \right) - \operatorname{erf} \left( \frac{\theta - \theta_0}{\Delta\theta} \right)}{\exp \left( -\frac{\Delta\theta^2}{4} \right) \cos \theta_0 - \operatorname{erf} \left( \frac{\theta_0}{\Delta\theta} \right)} \quad (4)
 \end{aligned}$$

407 where  $R, \theta, \phi$  are spherical coordinates,  $N_{D0} = 3.94 \times 10^{24} \text{ s}^{-1}$  is the molecular flow rate,  $v_s = 3.2 \text{ km/s}$  is the  
 408 exhaust velocity,  $v_m = 0.1 \text{ km/s}$  is the thermal speed,  $\Delta\theta = 30$  degrees is the plume angle and  $t_e = 60$   
 409 seconds is the duration of the engine burn. The number ratio of water molecules to nitrogen molecules  
 410 is 4:3. The simulation of the injection moves the source at  $7.3 \text{ km/s}$  with the nozzle pointed in the  
 411 ram/posigrade direction. More details on the modeling of molecular exhaust flow are provided by  
 412 Bernhardt [1979], Kaplan and Bernhardt [2010], and Bernhardt et al. [2012].

413 The Cygnus engine is operated for 60 seconds while moving horizontally at  $7.3 \text{ km/s}$ . The BT-4 engine  
 414 operated while pointed in the ram direction relative to the orbit of the satellite. In the neutral exhaust  
 415 model, the orbit is along the  $z$ -axis and the exhaust plume expands to form a cone in cylindrical  
 416 coordinates relative to the radial ( $r$ ) and axial ( $z$ ) directions. The plume model neglects the compensating  
 417 effects of the curvature of the orbit and the force of gravity. Figure 9 shows the neutral density at four  
 418 times (0.5, 1, 2 and 3 minutes) after the start of the burn. Charge exchange with the water vapor and  
 419 atomic oxygen ions produce supersonic  $\text{H}_2\text{O}^+$  pickup ions that drive the VLF wave amplification process.  
 420 The expanding cloud of water vapor is dense enough to yield energetic pickup ions several minutes after  
 421 the rocket motor stops (Figure 9).

422 The exhaust expansion model assumes that all the exhaust material vaporizes. Yu. V. Platova, A. I.  
 423 Semenovb, and B. P. Filippova [2011] have considered the condensation process of water vapors in the  
 424 exhaust plume of a rocket engine in the upper atmosphere. After formation, the ice particles evaporation  
 425 by heating during the release of latent heat of condensation, radiative heating, and energy losses to  
 426 emission. The re-evaporation process produces hypersonic water molecules down-stream from the

427 injection point and will increase the size of the wave amplification region. Re-evaporation may be  
 428 responsible for the extend duration of the VLF amplification after the Cygnus motor shuts off.

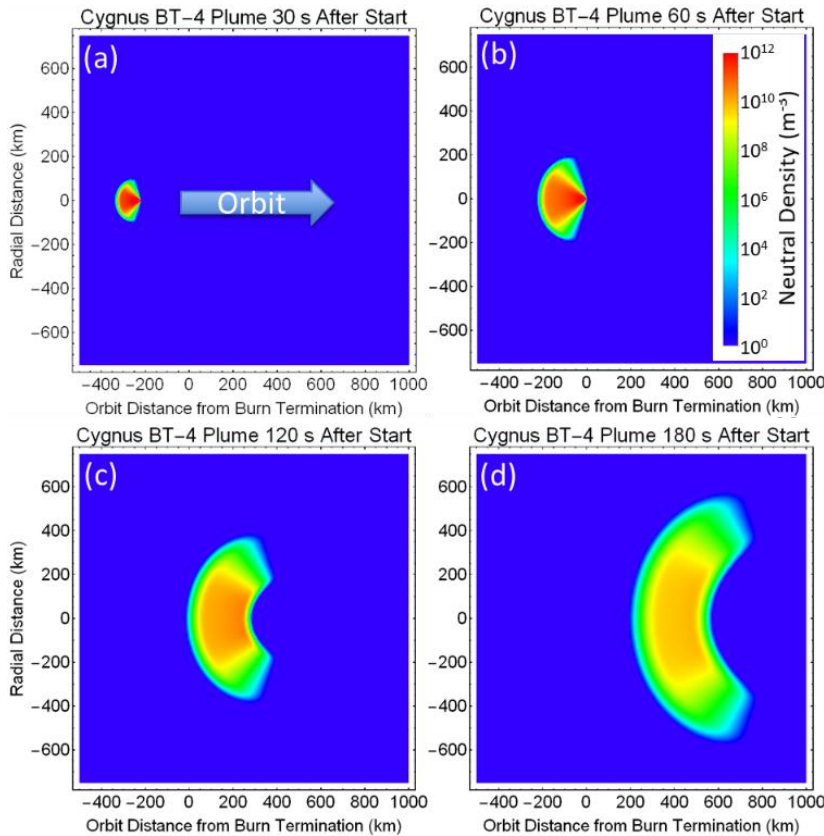


Figure 9. Neutral ( $H_2O$  plus  $N_2$ ) densities along the Cygnus orbit for a 60 second burn of the BT-4 motor when the motor is firing at (a)  $t = 30$  and (b)  $60$  s. After the motor shuts off, the plume becomes an expanding shell at (c)  $t = 120$  s and (d)  $t = 180$  s. The length of the plume along the orbit axis is identical to the length of the exhaust trail segments in Figure 2.

447

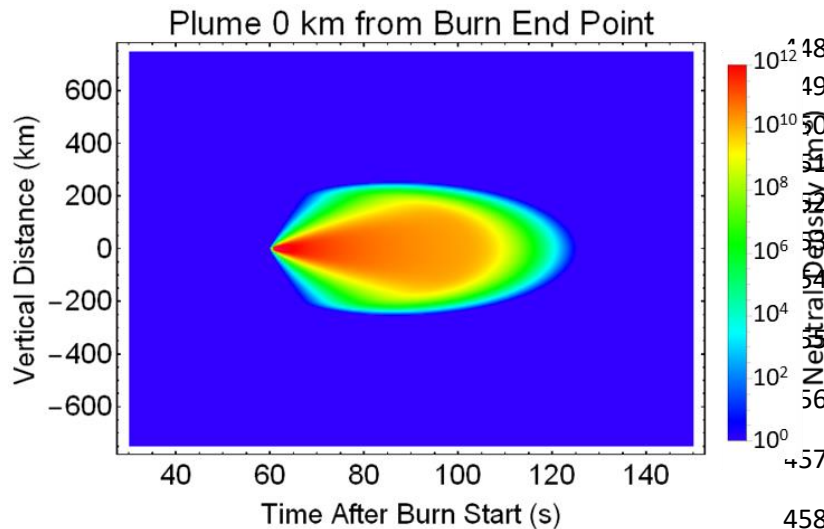


Figure 10. Exhaust molecule density at the  $L = 2.61$  field line containing the termination point of the Cygnus engine burn. The vertical distance is taken to be the  $z$ -coordinate along the magnetic field line.

459 Water ions produced at high speed become attached to magnetic field lines by moving in spiral orbits.  
 460 The density of the exhaust cloud on the field line at the termination point of the burn has the temporal  
 461 history illustrated in Figure 10. This cloud reacts with the ambient  $O^+$  and  $e^-$  species to give the product  
 462 ions and neutrals shown in equations (2) and (3). All the times,  $t$ , is relative to the burn start even though  
 463 the observations are presented relative to burn end. The cloud will be exciting the ion-ring distributions

464 well after  $t = 100$  seconds (or 40 seconds after the end of the 60-s burn). This explains the similar duration  
 465 for VLF wave amplification in the measured data of Figure 4.

466 The production of whistler mode amplification ions requires hypersonic flow of water ions. The ion  
 467 plasma expansion is computed using one-dimensional solution for flow along a magnetic field line  $\mathbf{B}$  in the  
 468  $z$ -direction. The ionized species are dispersed by plasma transport described by the equations of  
 469 continuity

$$470 \quad \frac{\partial n_1}{\partial t} + \frac{\partial}{\partial z}(n_1 v_{1z}) = -k_{1E} n_1 n_E \quad (4)$$

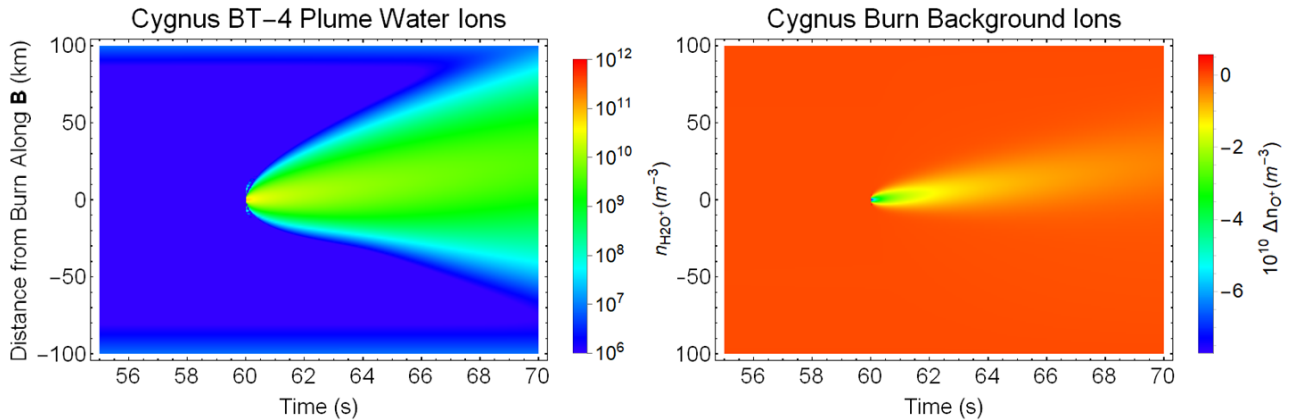
$$\frac{\partial n_2}{\partial t} + \frac{\partial}{\partial z}(n_2 v_{2z}) = k_{1E} n_1 n_E - k_{e2} n_2 n_e$$

471 and the equations of motion with an ambipolar electric-field setup by the electrons

$$472 \quad \frac{\partial v_{1z}}{\partial t} + \frac{1}{2} \frac{\partial v_{1z}^2}{\partial z} = -\frac{1}{n_1} \frac{\partial n_1}{\partial z} v_{T1}^2 - \frac{1}{n_e} \frac{\partial n_e}{\partial z} v_{Te1}^2 - g_0 \sin I - \nu_{1n} v_{1z} - \eta_{12} n_2 (v_{1z} - v_{2z})$$

$$\frac{\partial v_{2z}}{\partial t} + \frac{1}{2} \frac{\partial v_{2z}^2}{\partial z} = -\frac{1}{n_2} \frac{\partial n_2}{\partial z} v_{T2}^2 - \frac{1}{n_e} \frac{\partial n_e}{\partial z} v_{Te2}^2 - g_0 \sin I - \nu_{2n} v_{2z} - \eta_{12} n_1 (v_{2z} - v_{1z})$$

473 where the subscripts 1 and 2 refer to the respective ions  $O^+$  and  $H_2O^+$ ,  $k_{1E} = 2.49 \times 10^{-15} \text{ m}^3/\text{s}$  is the charge  
 474 exchange reaction rate between  $O^+$  and  $H_2O$  based on ion-neutral cross sections provide by Li et al. [1995],  
 475  $k_{e2} = 10^{-12}$  provided by Banks and Kockarts [1973],  $v_T$  is the thermal ion speed,  $g_0$  is gravitational  
 476 acceleration,  $\nu_{1n} = \nu_{2n} = 0.0038 \text{ s}^{-1}$  is the ion neutral collision frequency which based on the neutral MSIS  
 477 Model density at the injection altitude and  $\eta_{12} = 9.7 \times 10^{-14} \text{ m}^3/2$  is the momentum transfer factor for ion-  
 478 ion collisions from Banks and Kockarts [1973]. These equations are solved by the NRL SAMI2 and 3 models  
 479 along with the energy equation for the ions and electrons [Huba, Joyce and Fedder, 2000]. Here, these  
 480 equations are solved without ion inertia and advection, neglecting gravity, and excluding the effects of  
 481 the  $N_2$  molecule because of its slow reaction rate ( $10^{-18} \text{ m}^3/\text{s}$ ) with  $O^+$ .



482  
 483 Figure 11. Estimation of the pickup ion and ambient ion densities from solutions of continuity and  
 484 momentum equations with charge exchange chemistry and ion-electron recombination chemistry. The  
 485 origin of the distance axis is 480.9 km in altitude and the field line is located at the end of the burn. The  
 486 time is relative to the start of the 60-s burn.

487 The results of this simulation for the ion changes on the field line located at the end to the burn are shown  
 488 in Figure 11. The neutral density release presented in Figure 10 is used to react with the oxygen ions in  
 489 the ionosphere at 480 km altitude. The injected neutrals produce high-speed water ions that diffuse along  
 490 magnetic field lines. The oxygen ion hole produced by ion-molecule charge exchange and are filled-in by  
 491 field-aligned diffusion. The computed ion expansion rate is supersonic so the inertial and advection terms  
 492 in the momentum equations need to be included in future, more accurate solutions. Acoustic shock flow  
 493 is expected to slow the expansion of water ions along the magnetic field lines.

494 **5. Background Plasma Conditions Observed with the GPS Attitude and Position (GAP) sensor and**  
 495 **Magnetic Field (MGF) instrument on e-POP.**

496 Validation of the formation of hypersonic molecular ions is provided by measurements of the  
 497 recombination of these ions with electrons. This measurement is made with total electron content for  
 498 GPS signals passing through the modified ionosphere. The GPS Attitude and Position (GAP) sensors on  
 499 SWARM-E/e-POP are comprised of three working antennas located on the top of the SWARM-E/CASSIOPE  
 500 satellite and on the one antenna on the anti-RAM face of the satellite. These antennas feed five separate  
 501 GPS receivers for determination of total electron content (TEC) to any GPS satellite in view of the e-POP  
 502 sensor.

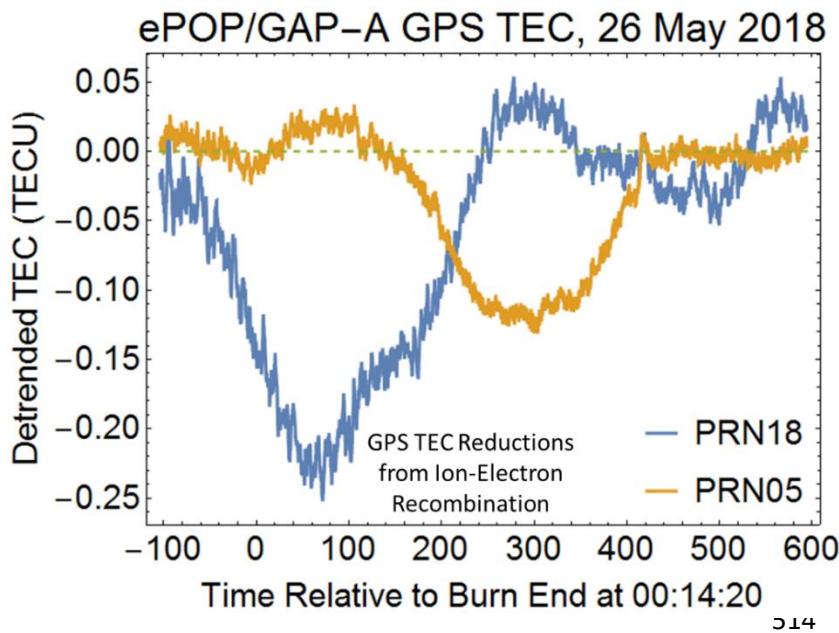


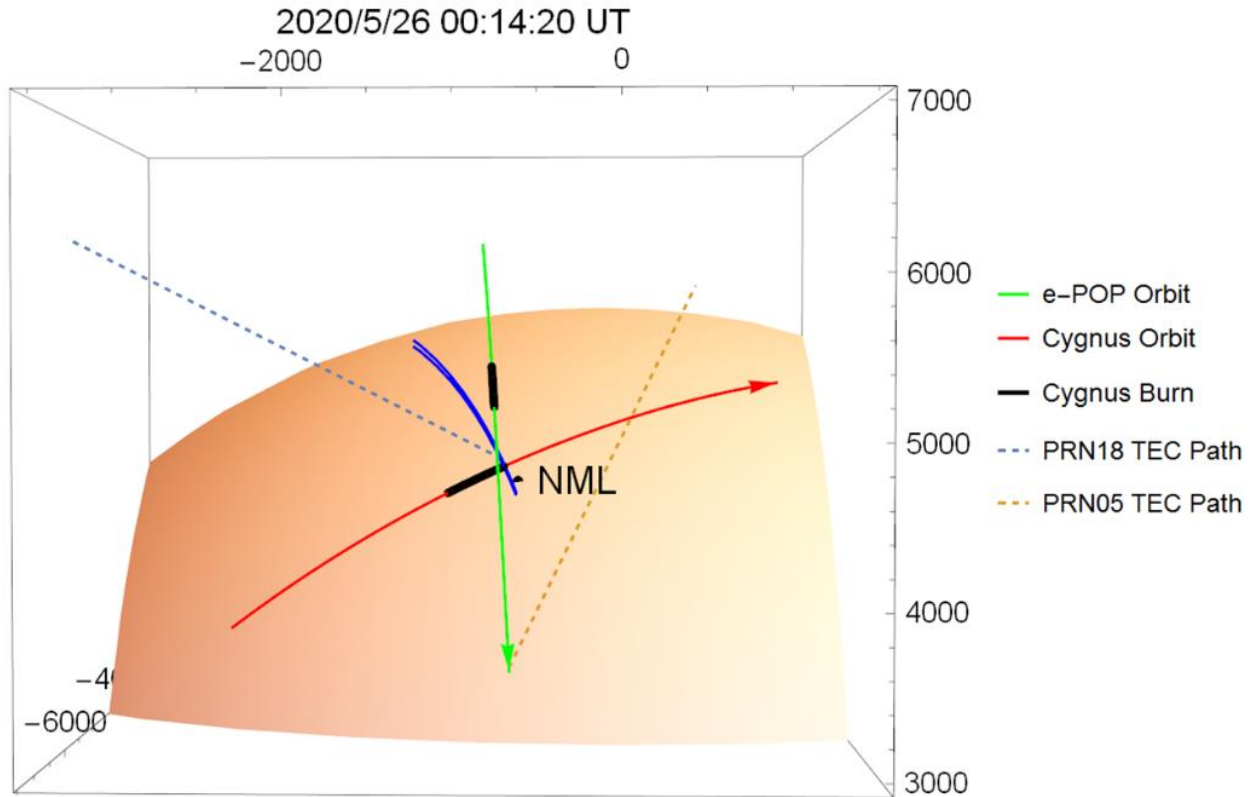
Figure 12. Measured deviations in integrated electron density (TEC) from GPS beacon satellites PRN18 and PRN 05.

515 The GAP instrument on e-POP serves two purposes for the NG-13 burn experiment. First, the GAP-A  
 516 (attitude) data register any changes in integrated electron density associated with electron-ion  
 517 recombination of the molecular ions produced by the charge exchange reactions (2). The recombination  
 518 process converts the molecular ions into neutrals with the reactions



520 as given in numerous papers on the creation of ionospheric holes including Bernhardt [1987]. The GAP-A  
 521 sensors recorded TEC along 6 separate paths to GPS satellites identified by their PRN number. Two of  
 522 these paths from PRN18 and PRN05 had TEC changes associated with the Cygnus engine burn (Figure 12).

523 These data are obtained by subtracting a third-order polynomial fit from the measured TEC over a period  
 524 of 1000 seconds. The minimum PRN18 and PRN05 TEC are measured 65 and 296 seconds, respectively,  
 525 after the end of the Cygnus burn. These are interpreted as evidence of molecular ion recombination for  
 526 Cygnus exhaust charge exchange species.



527 Figure 13. Overhead view of the e-POP/SWARM-E satellite N-S orbit (Green) and Cygnus W-E trajectory  
 528 (Red) relative to the burn times of the Cygnus BT-4 engine. The dashed lines from GAP to the PRN18  
 529 (Blue) and PRN05 (Orange) GPS satellites at times of when a minimum in the GAP TEC measured along the  
 530 line-of-sight paths. The magnetic field line at the end of the Cygnus burn is shown with a solid blue line.

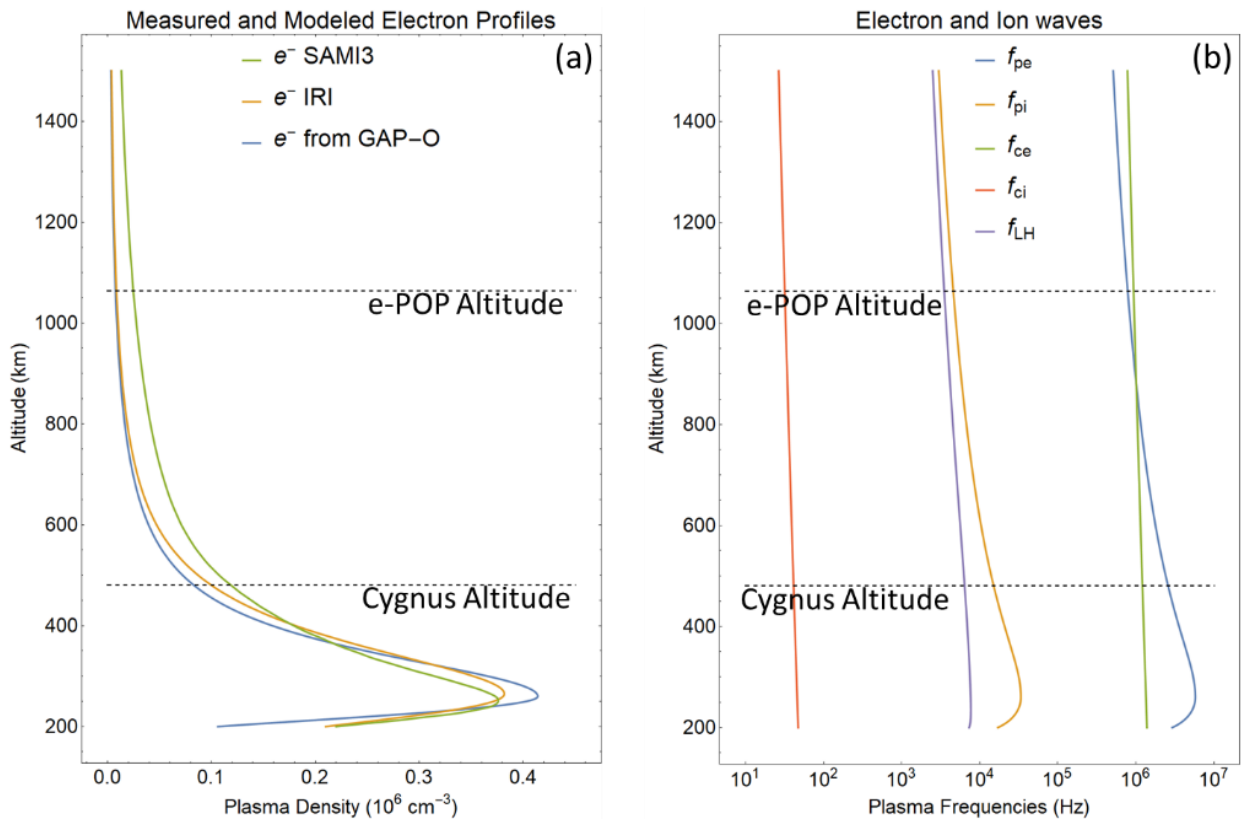
531 The time differences in measured TEC reductions are associated with the locations of the GPS satellites  
 532 relative to the motion of the GAP-A receiver on e-POP. Figure 13 shows the GPS line-of-sight  
 533 measurement geometry to the GAP sensor relative to the Cygnus and e-POP orbits and locations of the  
 534 Cygnus burn. The PRN18 path (Dashed-Blue Line) is much closer to the modified field line than the path  
 535 to PRN05. These measurements of plasma density reductions reinforce the proposition that molecular  
 536 ions are produced by charge exchange with the Cygnus exhaust followed by electron-ion recombination.  
 537 This recombination limits the effectiveness of spiraling ions to produce an amplification environment for  
 538 the whistler mode.

539 Another, equally important, use of the GAP instrument is to provide electron density profiles with the GPS  
 540 Occultation technique. The sensor (GAP-O) measures total electron content (TEC) along paths near the  
 541 limb of the earth. The slant TEC data are processed by an Abel Inversion (AI) technique to determine a  
 542 profile of the ambient, unmodified ionosphere. This profile compares well with the ionospheric densities  
 543 from the SAMI3 physics based model and IRI empirical model (Figure 14a). Based on these models, the

544 ion composition and concentration at the Cygnus and e-POP/SWARM-E satellite altitudes are determined  
 545 to be atomic oxygen ions with a density equal to that of the electrons.

546 The e-POP MGF instrument provides a magnetic field vector that closely matches the IGRF model of the  
 547 earth's magnetic field. There is no evidence of any MHD waves seen at frequencies below 40 Hz in the  
 548 MGF data.

549



550

551 Figure 14. Profiles of (a) electron densities derived from the NRL SAMI3 plasma model, the International  
 552 Reference Ionosphere Model (IRI), and GPS occultation measurements of TEC and (b) electron and ion  
 553 plasma frequency, electron and ion cyclotron frequency, and lower-hybrid frequency based on an electron  
 554 and  $O^+$ -ion plasma.

555 With accurate estimates of plasma density and composition along with magnetic field strength, the  
 556 plasma frequencies are computed in the ionosphere at the satellite locations (Figure 14b). The electron  
 557 whistler can be amplified by the Cygnus modified plasma in the frequency range between the ion  
 558 cyclotron frequency (41 Hz) and the electron cyclotron frequency (1.1 MHz). The frequency cutoff for  
 559 unducted whistler is the lower hybrid frequency at 6.45 kHz. The electron plasma frequency at Cygnus  
 560 altitude of 480 km is around 2.6 MHz. The background plasma parameters indicate that the two strongly  
 561 amplified frequencies, 300 Hz and 25.2 kHz were all whistler modes at both the amplification altitude (480  
 562 km) and the receiver altitude (1060 km). The time period for this amplification is labeled VLF and ELF  
 563 REDA in Figures D and G, respectively.

564 Based on the magnetic field and electron/ion density models, the relevant plasma frequencies can be  
 565 determined both at the Cygnus engine injection and at the e-POP RRI sensor altitudes (Table III). The  
 566 amplified coherent frequencies of 300 Hz and 25.2 kHz are between the ion gyro frequency and the  
 567 electron gyro frequencies near 40 Hz and 1.2 MHz, respectively. There is no direct coupling between the  
 568 amplified coherent waves and the lower hybrid frequency of 6.4 kHz. Figures Ca and Cb shows  
 569 intensification, after the Cygnus engine burn, at the incoherent emissions near lower hybrid (LH)  
 570 frequency which may be associated with amplification of existing non-ducted whistlers. The other  
 571 incoherent emission labeled SPWE near 13 kHz was also amplified for a period of about 120 seconds  
 572 starting 30 seconds after the start of the burn. This emission was attributed to finite  $k_z$  lower hybrid waves  
 573 at the spacecraft [Bernhardt, et al., 2020]. The parameters in Table III should aid future theoretical  
 574 research to understand the nonlinear amplification processes.

575 **Table III. NG13 Cygnus Experiment Wave Parameters**

| Plasma Wave Frequency     | Cygnus 480 km Altitude | e-POP 1060 km Altitude |
|---------------------------|------------------------|------------------------|
| Electron Plasma Frequency | 2.590 MHz              | 0.790 MHz              |
| Ion Plasma Frequency      | 0.151 MHz              | 0.046 MHz              |
| Electron Gyro Frequency   | 1.211 MHz              | 0.936 MHz              |
| Ion Gyro Frequency        | 41.3 Hz                | 31.9 Hz                |
| Low Hybrid Frequency      | 6.41 kHz               | 3.52 kHz               |

576

## 577 6. Whistler Mode Propagation in the Magneto-Plasma

578 The propagation of whistler modes between hemispheres is key to interpreting the RRI data from the  
 579 Cygnus NG-13 burn. The electron density along a field line determines the path of the electromagnetic  
 580 whistler waves. With validation provided by the GAP-O plasma profiles shown in Figure 14, the full  
 581 interhemispheric plasma densities are computed with the SAMI3 model for L shells ranging between L =  
 582 2 and 3. The ELF and VLF whistler mode rays are traced with an electromagnetic propagation code written  
 583 in Mathematica 12 based on numerical solution of by Hamilton's equations

$$584 \quad \frac{d\mathbf{r}}{d\tau} = \nabla_{\mathbf{k}} H(\mathbf{r}, \mathbf{k}), \quad \frac{d\mathbf{k}}{d\tau} = -\nabla_{\mathbf{r}} H(\mathbf{r}, \mathbf{k}), \quad \frac{dt}{d\tau} = \frac{dH(\mathbf{r}, \mathbf{k})}{d\omega} \quad (4)$$

585 for position, directional wave number, and time, respectively. The Hamiltonian is given by

$$586 \quad H(\mathbf{r}, \mathbf{k}) = \frac{1}{2} \left[ \frac{c^2}{\omega^2} \mathbf{k} \cdot \mathbf{k} - n^2(\mathbf{r}, \mathbf{k}, \omega) \right] \quad (5)$$

587 where the whistler mode refractive index

$$588 \quad n^2(\mathbf{r}, \mathbf{k}, \omega) = 1 - \frac{X(\mathbf{r}, \omega)}{1 - |\mathbf{Y}[\mathbf{k}]|/k} \quad \text{where } X = \frac{\omega_{pe}^2}{\omega^2}, Y = \frac{\Omega_{ce}}{\omega}, \omega_{pe}^2 = \frac{e^2 N_e(r)}{m_e \epsilon_0}, \Omega_{ce} = \frac{e\mathbf{B}}{m_e} \quad (6)$$

589 is a function of the respective plasma and gyro frequencies. The time delay function in (4) leads to the  
 590 definition of the group-delay refractive index given by  $n_g(\mathbf{r}, \mathbf{k}, \omega) = n(\mathbf{r}, \mathbf{k}, \omega) + \omega \frac{dn(\mathbf{r}, \mathbf{k}, \omega)}{d\omega}$ .

591 Yeh and Liu [1972], Bernhardt [1979], and Swanson [1989] give further details on the whistler mode ray  
 592 tracing process.

593

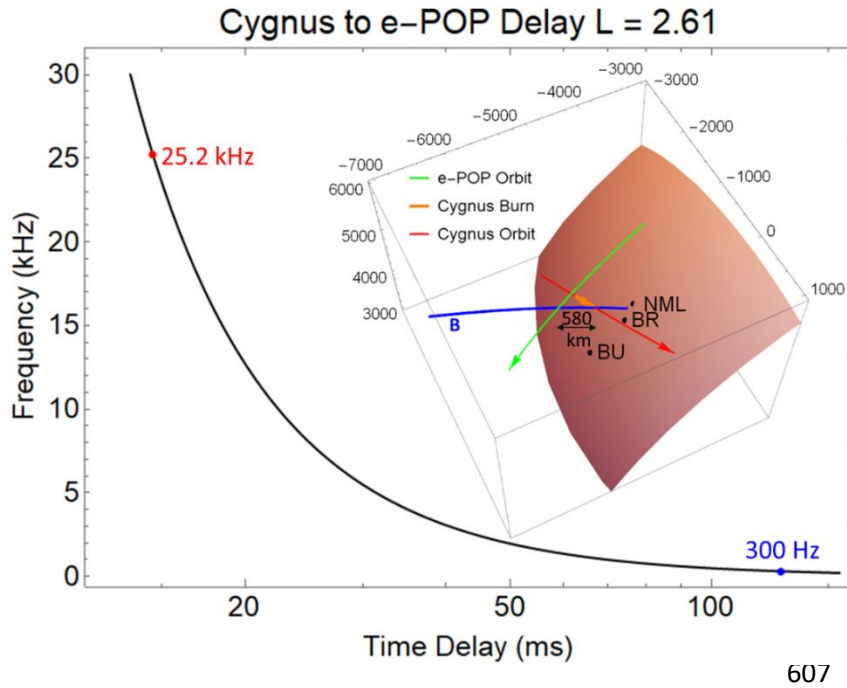


Figure 15. Whistler mode dispersion, with orbit geometry inset, showing time delays along the 580 km path from the Cygnus burn (orange) to the e-POP RRI sensor orbit (green) at the time of closest approach.

608 The important time delays for the amplified whistler modes are (1) from the amplification region (i.e.,  
 609 around Cygnus) to the receiver (i.e., RRI on e-POP) and (2) from one hemisphere to the other.  
 610 Computation of the whistler mode propagation requires the magnetic field model based on IGRF and a  
 611 description of the electron densities along the magnetic field lines. A good estimation of whistler  
 612 propagation delay is found by integration of the inverse group velocity along the magnetic field line using

613 
$$t_g = \int_s n_g(\mathbf{r}(s), \mathbf{k}, \omega) \frac{ds}{c}$$
 where  $c$  is the speed of light. This assumes that the ray path is confined to a

614 magnetic field line and that the wave normal direction is coincident with the direction of  $\mathbf{B}$ .

615 The calculated propagation times for a whistler excited near Cygnus to be received by RRI on SWARM-E  
 616 are 127 ms for 300 Hz and 15 ms for 25.2 kHz (Figure 15). The computed whistler group dispersion for  
 617 inter-hemispheric propagation along the dipole field line is illustrated in Figure 16. The one-hop time  
 618 delay for 300 Hz is 1.46 seconds and the delay at 25.2 kHz is 0.27 seconds. These times could be resolved  
 619 with the e-POP RRI with its sample rate at 16 microseconds.

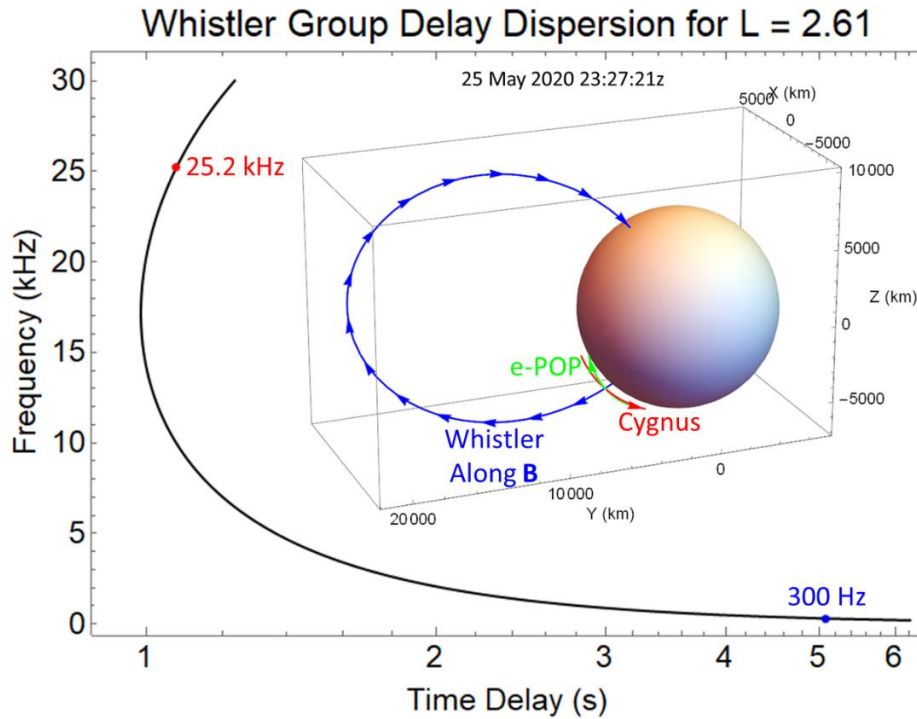


Figure 16. Group delays for amplified whistler mode waves propagating from the Cygnus orbit in the northern hemisphere to the bottom of the conjugate hemisphere ionosphere. The inset shows the magnetic field line associated with guiding the waves for multi-hop propagation.

636 Raytracing is employed to understand the fate of the amplified waves after they leave the Cygnus exhaust  
 637 region, couple into VLF field-aligned ducts, and propagate to the conjugate hemisphere. Whistler  
 638 modewaves can be guided by enhanced columns of plasma along magnetic field lines [Smith et al., 1960,  
 639 Helliwell, 1965, Angerami, 1970; Bernhardt and Park, 1977; Strangeways, 1981, Rudenchik, 1993]. The  
 640 gradients at the end of an enhancement duct are critical for determining whether the trapped ray will  
 641 reflect at or emerge from the endpoint. Thus, a whistler duct acts like a partially reflecting/transmitting  
 642 mirror for the portions of the trapped EM wave spectrum that echo from and penetrate through the duct  
 643 end region, respectively. The transmitted wave power propagates downward into the F-region and can  
 644 be received on the ground. A related duct feature is their capability to capture unducted whistlers at their  
 645 end points. This feature is critical for exciting ducts with whistler mode waves that eventually interact  
 646 with radiation belt particles [Burgess and Inan, 2012].

647 The coupling of whistler waves into VLF ducts has been modeled and explained by Bernhardt and Park  
 648 [1977]. An example of this coupling for the 300 Hz and 25.2 kHz waves in a duct above the Cygnus  
 649 amplified region is shown in Figure 17. The many rays for the ELF/VLF waves that have passed through  
 650 the bottomside ionosphere are refracted to the vertical by the large refractive index of the whistler mode  
 651 in the plasma. Some of these rays will pass through the rocket exhaust driven amplification (REDA) region  
 652 and may be captured by an ambient enhancement duct such as has been illustrated by the light-blue area in  
 653 Figure 17. This duct, which extends into the magnetosphere, was created by enhancing the electron  
 654 density associated with the light ions (H<sup>+</sup> and He<sup>+</sup>) in the SAMI 3 model [Huba and Joyce, 2010; Juba and  
 655 Krall, 2013] by 8% using the procedure of Bernhardt and Park [1977]. The density enhancement is formed  
 656 over a region perpendicular to the L = 2.61 magnetic field line with a Gaussian profile width of 0.06 in L.  
 657 This duct is consistent with observations made by Angerami [1970]. The whistler waves enter this duct  
 658 from the bottom with wave-normal directions nearly aligned with the earth's magnetic field. The ray  
 659 paths in Figure 17 are continuous but the nonlinear process in the REDA region may re-radiate plasma  
 660 waves with **k**-vectors in a spectrum of directions from a parametric amplification process. The

661 observations from the NG-13 Cygnus burn suggest that the amplification process produces a broad wave  
 662 number spectrum of waves from the source region that can propagate to the RRI sensor at 1064 km and  
 663 can couple efficiently into ducts above this altitude.

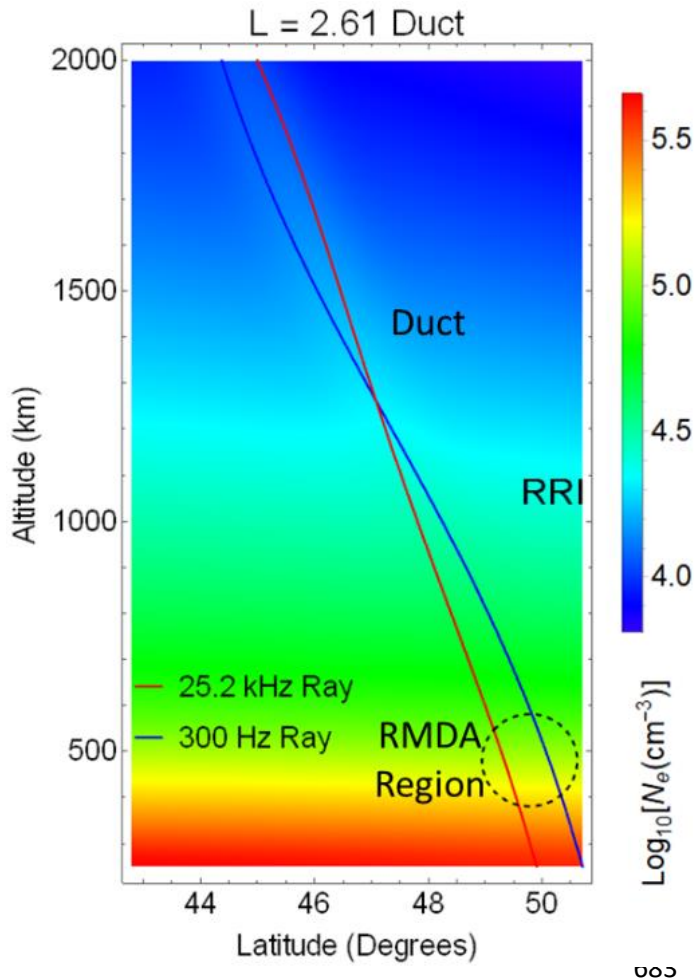
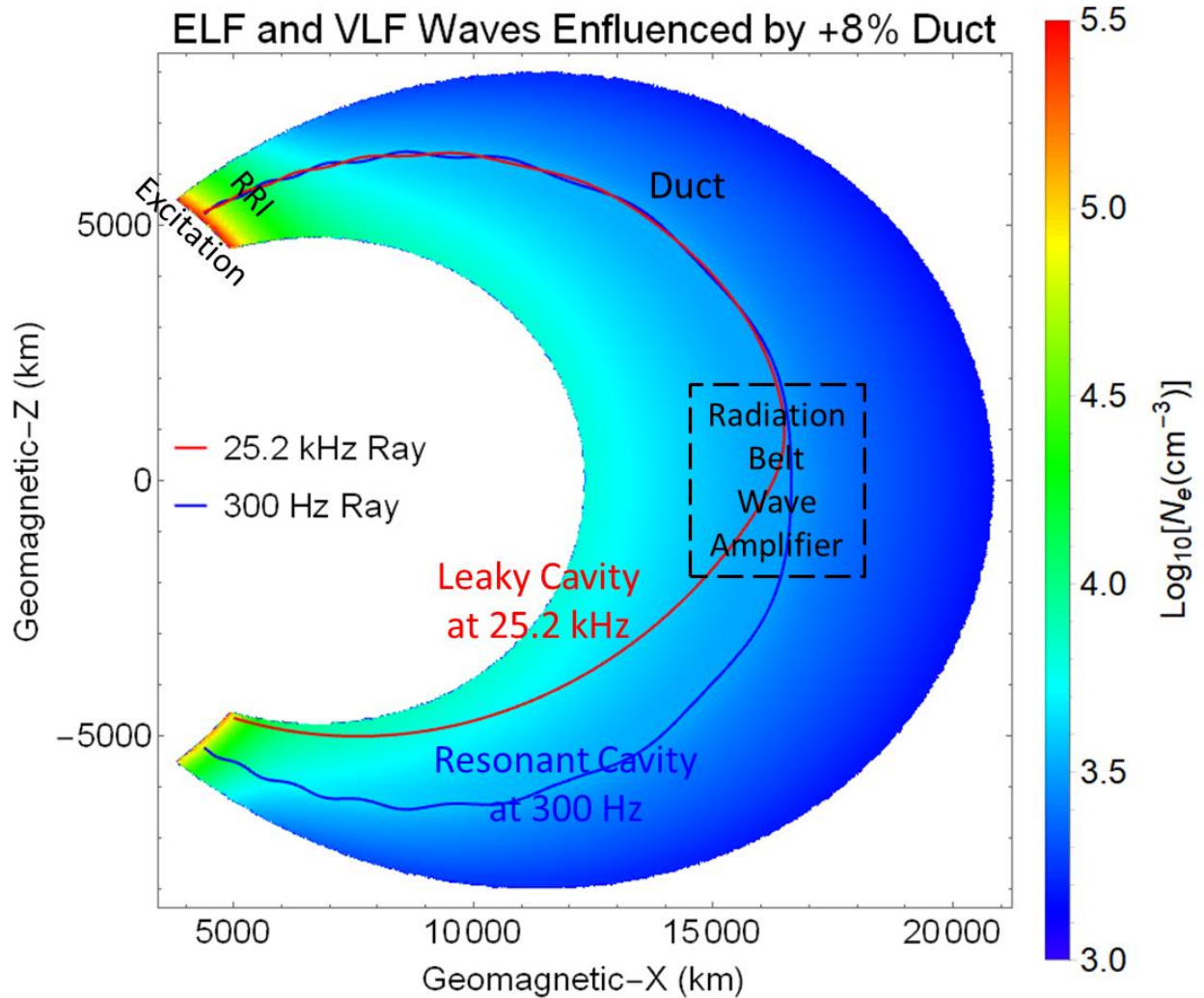


Figure 17. Two ELF (Blue) and VLF (Red) rays from ground sources pass through the F-region and propagate through the REDA region of active ions illustrated in Figure 11. The amplified waves couple into an  $L = 2.61$  enhancement duct extending down from the magnetosphere. Note that the duct is tilted by the magnetic dip angle of  $66^\circ$  and the RRI instrument on e-POP is located slightly to the north of the captured rays.

684 After an EM whistler is captured by a duct, it can be guided along magnetic field lines by the refractive  
 685 index gradients across the tube of enhanced plasma. Ducted whistlers with frequencies above one-half  
 686 the equatorial electron gyro frequency may leak out (i.e., become unducted) and may not reach the  
 687 conjugate hemisphere [Bernhardt, 1979]. This process is illustrated by the computed ray paths in Figure  
 688 18. The electron gyro frequency,  $f_{ce}$ , at the equator of the magnetic field line for the Cygnus burn is 47.1  
 689 kHz. Thus, a ducted 25.2 kHz signal from NML can follow the magnetic field line until it reaches the  
 690 equatorial region of the dipole field line where  $f_{ce}/2$  is 23.55 kHz and it leaks out [Red curve in Figure 18].  
 691 The amplified 25.2 kHz VLF waves are not expected to be ducted across the magnetic equator at  $L = 2.61$   
 692 and their 2-hop echoes are not expected to be seen at the e-POP RRI sensor.



693

694 Figure 18. Magnetosphericly ducted and partially-ducted whistler mode waves modeled on a field  
 695 aligned enhancement extending into the protosphere. Both the ELF (blue) and VLF (red) rays are guided  
 696 by the duct to the equatorial part of the magnetic field line at which point the duct becomes leaky for the  
 697 VLF wave. The 300 Hz ELF wave remains confined to the duct for either transmission or reflection at the  
 698 conjugate hemisphere. The ELF wave may be amplified multiple times by this reflection process. The 25.2  
 699 kHz VLF wave is amplified only by radiation belts in the cavity.

700 In contrast, the amplified and trapped 300 Hz signals will be ducted along the magnetic field lines [Blue  
 701 Curve in Figure 18] to produce multiple-hop echoes that could be observed at the RRI after the burn. The  
 702 300 Hz ELF echoes can have amplified interactions with the radiation belt particles on the  $L = 2.61$   
 703 magnetic field line and this process may lead to energetic electron precipitation.

704 The simulated absence of interhemispheric VLF propagation at 25.2 kHz and the much larger amplification  
 705 of the ELV (300 Hz) signal is consistent with the observations of the amplified signals observed by RRI on  
 706 e-POP. Figures C through G show that the 20 to 30 dB amplification of the 25.2 kHz VLF waves are only  
 707 observed for about 23 seconds after the end of the Cygnus burn. In contrast the 300 Hz ELF waves were  
 708 intensified by 50 dB for at least 180 seconds after termination of the burn [Figure 7]. This long duration

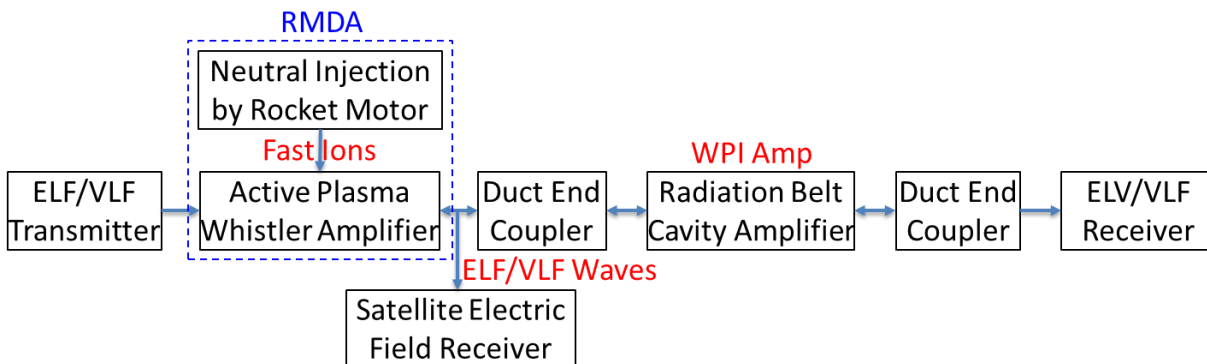
709 effect is attributed to excitation of an active ELF field-aligned resonator established between the two  
 710 reflection points at the ends of the duct.

711 We conclude that an echoing whistler train is set up after being initiated with the Cygnus burn  
 712 amplification of a ground based signal at 300 Hz. This signal excites a VLF whistler mode resonator  
 713 supported by amplification by cyclotron resonance with radiation belt particles trapped on the magnetic  
 714 field lines [Figure 18]. The energy of the resonant particles is computed from the cyclotron resonance  
 715 formula [Sa, 1989; Chang et al., 2014]

716 
$$\frac{\partial \theta}{\partial t} = -k_1 v_{\parallel} - \omega_1 + \omega_{ce} \text{ where } \omega_{ce} = \frac{eB_0}{m_e}, E_{e\parallel} = \frac{1}{2} m_e v_{\parallel}^2 .$$

717 When particles are in resonance with the whistler wave, the angular velocity  $\dot{\theta}$  goes to zero. For the 300  
 718 Hz whistler mode amplified by the Cygnus burn, the whistler mode dispersion equation gives  $k_1 =$   
 719  $0.0000173 \text{ m}^{-1}$  and the resonant electron energy is 8.24 MeV which has a flux of  $0.1 \text{ cm}^{-2} \text{ s}^{-1} \text{ sr}^{-1} \text{ keV}^{-1}$  on  
 720 an  $L = 3$  magnetic field line as measured with the Van Allen Belt Probes [Zhao et al. 2019a]. The 25.2 kHz  
 721 whistler has resonance with 21.5 keV electrons which have a flux a million times larger in the  $L = 3$   
 722 radiation belts. An optimum choice of frequency for the REDA experiment to induce radiation belt  
 723 amplification may be in the 2 to 6 kHz range for multiple-hop guiding by field aligned whistler ducts and  
 724 resonant interactions with large populations of energetic electrons.

725 Therefore, the REDA process may launch intense whistler waves with additional amplification by the  
 726 radiation belt environment. The complete system of ground EM transmissions propagating and amplified  
 727 by the Cygnus burn region with further amplification in the radiation belts is illustrated by the diagram in  
 728 Figure 19. This same type of process has been used for many years in laser amplifiers with and without  
 729 an optical cavity [Siegman, 1986]. The whistler mode cavity amplifier is usually excited by lightning with  
 730 pulse lengths on the order of seconds. Monochromatic waves transmitted from Siple Station, Antarctica  
 731 have produced 5 dB to 40 dB amplification with growth rates between 20 and 350 dB/s [Li et al., 2014].  
 732 Thus it is very reasonable for the radiation belt interactions to produce 20 dB cavity amplification for the  
 733 long duration ELF (300 Hz) signals as inferred here.



734  
 735 Figure 19. Plasma amplification of whistler mode with cavity excitation. EM waves from the ground VLF  
 736 transmitters are amplified by the REDA process before they couple into a field aligned duct that acts like  
 737 a cavity resonator. Leakage from the ends of the ducts should yield ground observable EM waves.

738

739 **7. Summary**

740 Using existing resources in space and on the ground, the first demonstration of rocket exhaust driven  
 741 amplification (REDA) of whistler mode waves occurred on 26 May 2020. The primary source of coherent  
 742 VLF waves was the U.S. Navy NML Transmitter at 25.2 kHz located in LaMoure, North Dakota. A region of  
 743 the topside ionosphere at 480 km altitude became an amplifying medium with a 60 second firing of the  
 744 Cygnus BT-4 engine. The rocket exhaust, injected as a neutral cloud moved perpendicular to field lines  
 745 that connected the NML transmitter to the VLF Radio Receiver Instrument (RRI) on e-POP/SWARM-E at  
 746 1080 km altitude. The 25.2 kHz VLF signal from NML was amplified by a factor of  $10^3$  in power (30 dB) for  
 747 a period 77 seconds as observed with the electric fields measurements by the RRI. A secondary source of  
 748 coherent ELF waves became amplified by a factor of  $10^5$  (50 dB) relative to a 300 Hz signal before the  
 749 engine burn. The 300 Hz ELF waves are of unknown origin but they were related to harmonics of 100 Hz  
 750 recorded by the RRI more the 600 seconds before the Cygnus burn. Extremely strong coherent emissions  
 751 and quasi-periodic bursts were observed in the 300 to 310 Hz frequency range for 200 seconds after the  
 752 release. The actual cavity excitation process may have lasted longer but the orbit of the SWARM-E/e-POP  
 753 moved the RRI sensor away from the wave emission region. Propagation analysis suggests that the 25.2  
 754 kHz VLF waves are less likely to be trapped in plasmaspheric ducts than the 300 Hz ELF band. The longer-  
 755 lived ELF modes may be the result of multi-hop whistler modes echoing between geomagnetic-conjugate  
 756 hemispheres.

757 The primary results of this paper are:

- 758 (1) Rocket exhaust driven amplification (REDA) was demonstrated when a Cygnus burn injected  
 759 hypersonic pickup ions across the propagation paths of ELF and VLF waves. The NG-13 Cygnus  
 760 Mission found a 0.5% to 25% conversion efficiency for plume kinetic energy conversion into  
 761 whistler wave energy. Both the nonlinear amplification process and the wave propagation mode  
 762 determine the electric-field strength at the 580 km range of the receiver. One theory behind this  
 763 amplification process involves parametrically driven interactions of the narrow-band source  
 764 waves and lower-hybrid waves. These LH waves are excited by the energetic ion distributions  
 765 formed when hypersonic neutral flow across the magnetic field lines. Other theoretical  
 766 mechanisms include conversion of the ring-ion distributions to electron velocity distributions that  
 767 lead to establishing a broad-band amplifying medium [Lee and Crawford, 1970].
- 768 (2) Existing ambient waves in the ELF or VLF frequency range can seed the amplification of low  
 769 frequency waves produced during chemical injection experiments. The NG-13 SEITE II experiment  
 770 described here occurred over a known ground source of 25.2 kHz. The ambient 300 Hz waves  
 771 from an unknown source produced the ELF signals 20 dB larger than the primary VLF source. Any  
 772 chemical injection or electron beam experiment designed to excite (as opposed amplify) VLF  
 773 waves should consider these seeding effects. A noise and emission survey in the release region  
 774 should be made before executing wave generation experiments.
- 775 (3) Future REDA experiments will use the electric field instrument in a **Medium or Low Gain Mode**.  
 776 The NG-13 REDA measurements used the RRI in High-Gain-Mode. As a result, the RRI preamplifier  
 777 was over-driven by the intensified ELF mode. In addition, modulation of the lower amplitude 25.2  
 778 kHz mode by the high amplitude 300 Hz was recorded. Fortunately, analysis has shown that the  
 779 compression of the 300 Hz and 25.2 kHz carriers of the signals were only 3 and 7 dB, respectively.  
 780 The **preamp** on RRI has a dynamic range of 120 dB and a gain setting of -11 (low), 19 (medium),  
 781 and 49 (high). The "hindsight is 20/20" conclusion for the preamp gain is that low or medium gain

782 levels should have been used to prevent electric field saturation. Since we know that the  
 783 amplified ELF or VLF signals are around 80 dB $\mu$ V/Hz, electric field receivers on other satellites can  
 784 be setup to prevent overloading.

785 (4) REDA and VLF excitation experiments with the Cygnus BT-4 (and other) rocket motors are being  
 786 planned for the near future. Several existing satellites with sensitive VLF receivers and energetic  
 787 particle detectors will be used to detect the amplified waves and their effects in space. Currently,  
 788 arrangements have been made with the University of Calgary, the Air Force Research Laboratory,  
 789 and the Institute for Space-Earth Environmental Research at Nagoya University to use wave and  
 790 particle instruments on the CASSIOPE/SWARM-E/ePOP (Enhanced Polar Outflow Probe), DSX  
 791 (Demonstration and Science Experiments), and ARASE (Exploration of Energization and Radiation  
 792 in Geospace) satellites, respectively. Multiple sensor satellites greatly enhance the probability of  
 793 having an alignment of ground transmitter, the Cygnus burn region and spaced-based VLF  
 794 receivers near a common magnetic field line. Strong correlations between ground NAA VLF  
 795 transmissions at 17.8 kHz and >27 keV electron fluxes were observed by Imhof et al. [1983] using  
 796 the Stimulated Emission of Energetic particles (SEEP) detectors on the S81-1 satellite. The space-  
 797 based measurements of energetic electron flux enhancements will be much larger after 30 dB  
 798 amplification of the NAA signal using REDA.

799 (5) The NG-13 REDA experiment had operational ground receivers recording signals from NML to try  
 800 to detect Chemical-release-induced electron precipitation (cep) and simultaneous VLF emissions  
 801 in space and on the ground. This is similar to the detection of lightning-induced electron  
 802 precipitation (lep) as reported by many authors including Smith, Inan, and Carpenter [1985],  
 803 Peter and Inan [2007] and Cotts [2011]. A few seconds after the Cygnus burn at 00:13:20,  
 804 transient VLF phase changes were detected by the UF ELF/VLF receiver system at Chistochina, AK  
 805 and the GIT VLF/LF receiver at Burden, KS. The phase change was 0.2 degree for about 20 seconds  
 806 and it is not significant based on signal to noise and in comparison to lightning-induced electron  
 807 precipitation (lep) events with 10-degree changes in phase. In addition, NG-13 REDA took place  
 808 during the day when D-region absorption makes the earth-ionosphere-waveguide insensitive to  
 809 detection of precipitation events. Future cep experiments will favor Cygnus burns during the  
 810 night when ionospheric waveguide attenuation is at a minimum.

811 (6) The REDA technique is relatively inexpensive only requiring coordination and preparation of the  
 812 Cygnus vehicle for activities after undocking from the Space Station. As such, REDA can be added  
 813 to any space mission designed to fly devices, such as coherently driven antennas (e.g. DSX) and  
 814 electron beams (i.e., PIE), on satellites. Future REDA experiments will also be conducted with and  
 815 without external sources of ELF/VLF waves. The neutral-cloud-injection speed from Cygnus can  
 816 be increased from 4.2 km/s to 10.5 km/s with a retrograde burn, which adds the spacecraft  
 817 velocity to the exhaust speed. The added kinetic energy may be sufficient to excite large  
 818 amplitude VLF waves using the theory proposed by Ganguli [2007].

819 (7) A critical point of this paper is that theory is not needed as a strong motivator for chemical  
 820 injection experiments to launch whistler modes for plasma turbulence studies. With the flexibility  
 821 of the Cygnus-like neutral injections with thruster attitude at any angle between prograde and  
 822 retrograde, the injection power can range between 1.3 MW and 8.3 MW. The injection altitude  
 823 can be chosen between 380 and 480 km to determine impact of collisions and ambient O<sup>+</sup> density  
 824 on the production of pickup ions. For a typical three week period after undocking from the ISS, 5

825 REDA experiments can be conducted before the end of a Cygnus mission. Supporting theory can  
826 be explored after measurements are made.

827 Acknowledgments. The work at the Naval Research Laboratory was provided under the NRL 6.1 Base  
828 Program. Support has been provided to NASA/JSC and Northrup Grumman working with MIT/LL to  
829 operate the Cygnus BT4 thruster. The European Space Agency's Third Party Mission Program supports  
830 the e-POP instruments on the CASSIOPE/SWARM-E satellite. All data used in this paper is available from  
831 the e-POP Data Center at <https://epop-data.phys.ucalgary.ca/>.

### 832 **References**

833 Angerami, J.J. (1970), Whistler Duct Properties Deduced from VLF Observations Made with the Ogo 3  
834 Satellite near the Magnetic Equator, *J. Geophys. Research Space physics*, 75, 6115-6135, 1970

835 Banks, P.M., and G. Kockarts, **Aeronomy**, Academic Press, 1973.

836 P. A. Bernhardt and C. G. Park (1977), Protonospheric-Ionospheric Modeling of VLF Ducts, 82, *Journal Of*  
837 *Geophysical Research*, 82, 5222-5230.

838 Bernhardt, P.A. (1979), Theory and analysis of the 'super whistler', *J. Geophys. Res.*, 84, pp. 5131-5142.

839 Bernhardt, P.A. (1987), A Critical Comparison of Ionospheric Depletion Chemicals, *Journal of Geophysical*  
840 *Research*, 92, pp 4617-4628, MAY 1, 1987

841 Bernhardt, P.A., M. P. Sulzer (2004), Incoherent scatter measurements of ring-ion beam distributions  
842 produced by space shuttle exhaust injections into the ionosphere, *Journal of Geophysical Research*, VOL.  
843 109, A02303, doi:10.1029/2002JA009693.

844 Bernhardt, P.A., J. O. Ballenthin, J. L. Baumgardner, A. Bhatt, I. D. Boyd, J. M. Burt, R. G. Caton, A. Coster, P.  
845 J. Erickson, J. D. Huba, G. D. Earle, C. R. Kaplan, J. C. Foster, K. M. Groves, R. A. Haaser, R. A. Heelis, D. E.  
846 Hunton, D. L. Hysell, J. H. Klenzing, M. F. Larsen, F. D. Lind, T. R. Pedersen, R. F. Pfaff, R. A. Stoneback, P. A.  
847 Roddy, S. P. Rodriguez, G. S. San Antonio, P. W. Schuck, C. L. Siefring, C. A. Selcher, S. M. Smith, E. R. Talaat,  
848 J. F. Thomason, R. T. Tsunoda, and R. H. Varney (2012), Ground and Space-Based Measurement of Rocket  
849 Engine Burns in the Ionosphere, *IEEE Transactions on Plasma Science*, 40, 1267.

850 Bernhardt, P.A., M. K. Griffin, W. C. Bougas, A. D. Howarth, H. G. James, C. L. Siefring and S. J. Briczinski  
851 (2020), Satellite Observations of Strong Plasma Wave Emissions with Frequency Shifts Induced by an  
852 Engine Burn from the Cygnus Spacecraft, Submitted to *Radio Science*.

853 Borovsky JE and Delzanno GL (2019), Active Experiments in Space: The Future, *Front. Astron. Space Sci.*  
854 6:31, doi:10.3389/fspas.2019.00031

855 W. C. Burgess, U. S. Inan (2012), The role of ducted whistlers in the precipitation loss and equilibrium flux  
856 of radiation belt electrons, *Journal of Geophysical Research: Space Physics*, 10.1029/93JA01202, 98, A9,  
857 (15643-15665).

858 Carlsten, B.E., P.L. Colestock, G.S. Cunningham, G.L. Delzanno, E.E. Dors, M.A. Holloway, C.A. Jeffery, J.W.  
859 Lewellen, Q.R. Marksteiner, D.C. Nguyen, G.D. Reeves, and K.A. Shipman, Radiation-Belt Remediation  
860 Using Space-Based Antennas and Electron Beams, *IEEE Transactions on Plasma Science*, 47, 2045, 2019

- 861 Carlsten, B.E. , P.L. Colestock, G.S. Cunningham , G.L. Delzanno, E.E. Dors , M.A. Holloway, C.A. Jeffery,  
862 J.W. Lewellen, Q.R. Marksteiner, D.C. Nguyen, G.D. Reeves , and K.A. Shipman, Response to Comment on  
863 "Radiation-Belt Remediation Using Space-Based Antennas and Electron Beams" by G. Ganguli and C.  
864 Crabtree, IEEE Transactions on Plasma Science, VOL. 48, NO. 2, Feb 2020.
- 865 Chang, S.S., S.S. Chang, B.B. Ni, J. Bortnik, C. Zhou, Z.Y. Zhao, J.X. Li, and X.D. Gu, Resonant scattering of  
866 energetic electrons in the plasmasphere by monotonic whistler-mode waves artificially generated by  
867 ionospheric modification, Ann. Geophys., 32, 507–518, 2014.
- 868 Cohen, M. B., and M. Golkowski (2013), 100 days of ELF/VLF generation via HF heating with HAARP, J.  
869 Geophys. Res. Space Physics, 118, 6597–6607, doi:10.1002/jgra.50558.1.
- 870 Cotts, B.R.T., Global Quantification of Lightning-induced Electron Precipitation Using Very Low Frequency  
871 Remote Sensing, PhD Dissertation, Stanford University, 2011.
- 872 Ganguli, G., Rudakov, L., Mithaiwala, M. & Papadopoulos, K. Generation and evolution of intense ion  
873 cyclotron turbulence by artificial plasma cloud in the magnetosphere. J. Geophys. Res. 112, A06231  
874 (2007).
- 875 Ganguli, G., Crabtree, C., Mithaiwala, M., Rudakov, L., and Scales, W. (2015), Evolution of lower hybrid  
876 turbulence in the ionosphere. Phys. Plasmas. 22:112904. doi:10.1063/1.4936281
- 877 Ganguli, G., Crabtree, C. E., Fletcher, A. C., Rudakov, L., Richardson, A. S., Huba, J., et al. (2019).  
878 Understanding and harnessing the dual electrostatic/electromagnetic character of plasma turbulence in  
879 the near-earth space environment. Journal of Geophysical Research: Space Physics, 124,  
880 <https://doi.org/10.1029/2019JA027372>.
- 881 Ganguli, G. and C. Crabtree, Comment on "Radiation-Belt Remediation Using Space-Based Antennas and  
882 Electron Beams" by Carlsten et al., IEEE Transactions on Plasma Science, VOL. 48, NO. 2, February 2020
- 883 Golkowski, M., V. Harid and P. Hosseini, Review of Controlled Excitation of Non-linear Wave-Particle  
884 Interactions in the Magnetosphere, Front. Astron. Space Sci., 07 February 2019  
885 <https://doi.org/10.3389/fspas.2019.00002>.
- 886 Hayosh, M., D. L. Pasmanik, A. G. Demekhov, O Santolik, Michel Parrot, et al. (2013). Simultaneous  
887 observations of quasi-periodic ELF/VLF wave emissions and electron precipitation by DEMETER satellite:  
888 A case study. Journal of Geophysical Research Space Physics, 2013, 118, pp.4523-4533.
- 889 Helliwell, R. A, Whistlers and Related Ionospheric Phenomena, Stanford University Press. Stanford. CA.  
890 1965.
- 891 R. A. Helliwell, Active very low frequency experiments on the magnetosphere from Siple Station,  
892 Antarctica, Phil. Trans. R. Soc. Lond. B. 279, 213-224 (1977).
- 893 J. D. Huba and G. Joyce, J. A. Fedder (2000), SAMI2 is Another Model of the Ionosphere (SAMI2)- A new  
894 low-latitude ionosphere model , Journal of Geophysical Research, VOL. 105, NO. A10, PAGES 23,035-  
895 23,053.
- 896 Huba, J.D. and G. Joyce (2010), Global modeling of equatorial plasma bubbles, Geophys. Res. Lett. 37,  
897 L17104, doi:10.1029/2010GL044281.

- 898 Huba, J.D. and J. Krall (2013), Modeling the plasmasphere with SAMI3, *Geophys. Res. Lett.* 40,  
899 doi:10.1029/2012GL054300.
- 900 W. L. Imhof, J. B. Reagan, H. D. Voss, E. E. Gaines, D. W. Datlowe, J. Mobilia, R. A. Helliwell, U. S. Inan, J.  
901 Katsufakis, and R. G. Joiner, "Direct observation of radiation belt electrons precipitated by the controlled  
902 injection of VLF signals from a ground-based transmitter," *J. Geophys. Res.*, vol. 10, no. 4, pp. 361–364,  
903 1983.
- 904 James, H.G. (2006) A Digital Radio Receiver for Ionospheric Research. In *Characterizing the Ionosphere*  
905 (pp. 23-1 – 23-16). Meeting Proceedings RTO-MP-IST-056, Paper 23. Neuilly-sur-Seine, France: RTO.  
906 Available from: <http://www.rto.nato.int/abstracts.asp>.
- 907 James, H.G., King, E.P., White, A. et al. The e-POP Radio Receiver Instrument on CASSIOPE. *Space Sci. Rev.*  
908 189, 79–105 (2015). <https://doi.org/10.1007/s11214-014-0130-y>
- 909 C. R. Kaplan and P. A. Bernhardt, "The effect of an altitude-dependent background atmosphere on space  
910 shuttle engine burn plumes," *J. Rockets Spacecraft*, vol. 47, pp. 700–704, 2010, DOI:10.2514/1.49339.
- 911 Kintner, P.M., R. Brittain, M. C. Kelley, D. C. Carpenter, and M. J. Rycroft, In situ measurements of  
912 transionospheric VLF waves injection, *J. Geophys. Res.*, 88, 7065, 1983.
- 913 Lee, J.C. and F. W. Crawford, Stability Analysis of Whistler Amplification, *J. Geophys. Res., Space Phys.*, 75,  
914 85-96, 1970.
- 915 Li, J. D., M. Spasojevic, V. Harid, M. B. Cohen, M. Gołkowski, and U. Inan (2014), Analysis of  
916 magnetospheric ELF/VLF wave amplification from the Siple Transmitter experiment, *J. Geophys. Res.*  
917 *Space Physics*, 119, 1837–1850, doi:10.1002/2013JA019513
- 918 Li, X., Y.-L. Huang, G. D. Flesch, and C. Y. Ng (1995), Absolute total cross sections for the ion-molecule  
919 reaction  $O^+(^4S_o) + H_2O$ , *J. Chem. Phys.*, 102, 5100–5101, doi:10.1063/1.469561.
- 920 Ma, Q., Mourenas, D., Li, W., Artemyev, A., & Thorne, R. M. (2017). VLF waves from ground-based  
921 transmitters observed by the Van Allen Probes: Statistical model and effects on plasmaspheric electrons.  
922 *Geophysical Research Letters*, 44, 6483–6491. <https://doi.org/10.1002/2017GL073885>.
- 923 Maxworth, A., G. Hussey and M.V. Gołkowski (2020), Coexistence of Lightning Generated Whistlers, Hiss  
924 and Lower Hybrid Noise Observed by e-POP (SWARM-E)–RRI, *Atmosphere*, 11, 177;  
925 doi:10.3390/atmos11020177.
- 926 Meredith, N. P., Horne, R. B., Clilverd, M. A., & Ross, J. P. J.. (2019), An investigation of VLF transmitter  
927 wave power in the inner radiation belt and slot region. *Journal of Geophysical Research: Space Physics*,  
928 124, 5246–5259. <https://doi.org/10.1029/2019JA026715> .
- 929 Platov, Y.V., Semenov, A.I. & Filippov, B.P. Condensation of combustion products in the exhaust plumes  
930 of rocket engines in the upper atmosphere. *Geomagn. Aeron.* 51, 550 (2011).  
931 <https://doi.org/10.1134/S0016793211040153>
- 932 R. Pradipta, A. Labno, M. C. Lee, W. J. Burke, M. P. Sulzer, J. A. Cohen, L. M. Burton, S. P. Kuo,5 and D. L.  
933 Rokusek, Electron precipitation from the inner radiation belt above Arecibo, *Geophysical Research Letters*,  
934 VOL. 34, L08101, doi:10.1029/2007GL029807, 2007

- 935 Ross, J. P. J., Meredith, N. P., Glauert, S. A., Horne, R. B., & Clilverd, M. A. (2019). Effects of VLF transmitter  
936 waves on the inner belt and slot region. *Journal of Geophysical Research: Space Physics*, 124, 5260–5277,  
937 <https://doi.org/10.1029/2019JA026716>
- 938 Parrot, M., Sauvaud, J., Berthelier, J., & Lebreton, J. (2007). First in-situ observations of strong ionospheric  
939 perturbations generated by a powerful VLF ground-based transmitter. *Geophysical Research Letters*, 34,  
940 L11111. <https://doi.org/10.1029/2007GL029368>
- 941 Peter, W. B., and U. S. Inan (2007), A quantitative comparison of lightning-induced electron precipitation  
942 and VLF signal perturbations, *J. Geophys. Res.*, 112, A12212, doi:10.1029/2006JA012165
- 943 Rudenchik, E. A. (1993), Trapping and Propagation of VLF Waves in Ducts: An Analytical Approach, *Planet.*  
944 *Space Sci.*, 41. pp. 619-631.
- 945 Sa, L. A. D., A cyclotron resonance mechanism for very-low-frequency whistler-mode sideband wave  
946 radiation. I - Introduction and description of external resonances, *Journal of Applied Physics*, 66, 3482-  
947 3514, 1989.
- 948 Scherbarth, Mark, Durand Smith, Aaron Adler, Janet Stuart, Greg Ginet, "AFRL's Demonstration and  
949 Science Experiments (DSX) mission." *Solar Physics and Space Weather Instrumentation III*. Ed. Silvano  
950 Fineschi & Judy A. Fennelly. San Diego, CA, USA: SPIE, 2009. 74380B-10. © 2009 SPIE—The International  
951 Society for Optical Engineering.
- 952 Siegman, A.E., *Lasers*, University Science Books, 1986.
- 953 Smith, A J, Carpenter DL, Inan US, Whistler-triggered VLF noise bursts observed on the DE-1 satellite and  
954 simultaneously at Antarctic ground stations, *Annales Geophysicae*, 3, 81–88, 1985.
- 955 Smith, R. L., Helliwell. R. A. and Yahroff (1960), I. W., A theory of whistler in field-aligned columns of  
956 enhanced ionization. *J. Geophys. Res.*, 65, 815.
- 957 Strangeways, H.J., Trapping of whistler-mode waves in ducts with tapered ends, *Journal of Atmospheric*  
958 *and Terrestrial Physics*, 10.1016/0021-9169(81)90022-2, 43, 10, (1071-1079), (1981).
- 959 Storey, L.R.O., An Investigation of Whistling Atmospheric, *Phil. Trans. Roy. Soc. London Ser. A*, 246, 113,  
960 1953.
- 961 Swanson, D.G., **Plasma Waves**, Academic Press, p. 59, 1989.
- 962 Yeh, K.C., and C.H. Liu, *Theory of Ionospheric Waves*, Academic Press, p. 239, 1972.
- 963 Zhao, H., Johnston, W. R., Baker, D. N., Li, X., Ni, B., Jaynes, A. N., et al. (2019a). Characterization and  
964 evolution of radiation belt electron energy spectra based on the Van Allen Probes measurements. *Journal*  
965 *of Geophysical Research: Space Physics*, 124, 4217–4232. <https://doi.org/10.1029/2019JA026697>
- 966 Zhao, S., Zhou, C., Shen, X. H., & Zhima, Z. (2019b). Investigation of VLF transmitter signals in the  
967 ionosphere by ZH-1 observations and full-wave simulation. *Journal of Geophysical Research: Space*  
968 *Physics*, 124, 4697–4709. <https://doi.org/10.1029/2019JA026593>

969 Záhlava, J., Němec, F., Pincon, J. L., Santolík, O., Kolmašová, I., & Parrot, M. (2018). Whistler influence on  
970 the overall very low frequency wave intensity in the upper ionosphere. *Journal of Geophysical Research:*  
971 *Space Physics*, 123, 5648–5660. <https://doi.org/10.1029/2017JA025137>